AGU PUBLICATIONS

JGR

Journal of Geophysical Research: Atmospheres

RESEARCH ARTICLE

10.1002/2014JD022448

Radiosonde observations of gravity waves in the lower stratosphere over Davis, Antarctica

D. J. Murphy[1], S. P. Alexander[1], A. R. Klekociuk[1], P. T. Love[1], and R. A. Vincent[2]

[1]Climate Processes and Change, Australian Antarctic Division, Department of the Environment, Kingston, Tasmania, Australia, [2]Department of Physics, University of Adelaide, Adelaide, South Australia, Australia

Key Points:
- Gravity waves in the Antarctic stratosphere are characterized
- Sources for downward propagating wintertime gravity waves are investigated

Correspondence to:
D. J. Murphy,
damian.murphy@aad.gov.au

Citation:
Murphy, D. J., S. P. Alexander, A. R. Klekociuk, P. T. Love, and R. A. Vincent (2014), Radiosonde observations of gravity waves in the lower stratosphere over Davis, Antarctica, *J. Geophys. Res. Atmos.*, *119*, 11,973–11,996, doi:10.1002/2014JD022448.

Received 14 AUG 2014
Accepted 15 OCT 2014
Accepted article online 20 OCT 2014
Published online 10 NOV 2014

Abstract Radiosonde observations made from Davis station, Antarctica, (68.6°S, 78.0°E) between 2001 and 2012 are used to compile a climatology of lower stratosphere inertial gravity wave characteristics. Wavelet analysis extracts single wave packets from the wind and temperature perturbations. Wavelet parameters, combined with linear gravity wave theory, allow for the derivation of a wide range of wave characteristics. Observational filtering associated with this analysis preferentially selects inertial gravity waves with vertical wavelengths less than 2–3 km. The vertical propagation statistics show strong temporal and height variations. The waves propagate close to the horizontal and are strongly advected by the background wind in the wintertime. Notably, around half of the waves observed in the stratosphere above Davis between early May and mid-October propagate downward. This feature is distributed over the observed stratospheric height range. Based on the similarity between the upward and downward propagating waves and on the vertical structure of the nonlinear balance residual in the polar winter stratosphere, it is concluded that a source due to imbalanced flow that is distributed across the winter lower stratosphere best explains the observations. Calculations of kinetic and potential energies and momentum fluxes highlight the potential for variations in results due to different analysis techniques.

1. Introduction

The importance of gravity waves to the dynamics of the middle atmosphere has long been recognized [*Holton*, 1983]; however, observations to quantitatively constrain their forcing are still lacking [*Alexander et al.*, 2010]. Meridional circulations that affect the dynamical and thermal state of the southern polar winter stratosphere are principally driven by gravity waves due to a dearth of planetary wave forcing in the Southern Hemisphere at that time [*Garcia and Boville*, 1994]. Gravity waves have horizontal scales that require parameterization in numerical models of the atmosphere. As a result, representation of the southern polar stratosphere is dependent on the quality of the gravity wave parameterization employed by the model which, typically, lacks physical constraint. This effect is felt most dramatically in the springtime stratosphere which is typically >5 K too cold [*Butchart et al.*, 2011]. Further observations of southern polar gravity waves are needed to improve physical constraints and model parameterization schemes.

The utility of radiosonde data for gravity wave studies was demonstrated by *Allen and Vincent* [1995], who used Australian radiosonde temperature perturbations to compile a climatology of gravity wave activity. *Hamilton and Vincent* [1995] suggested that wind and temperature data be permanently archived at the high time resolution available from the sondes (instead of at individual flight levels). Horizontal wind information was added to sonde data sets, providing the catalyst for more extensive analyses [e.g., *Vincent et al.*, 1997]: vertical propagation direction was extracted from the sense of rotation of the wind, and the wind components and temperature perturbations were used to obtain the direction of wave propagation. Intrinsic and ground-based wave characteristics also became available.

Hodographs and the phase variation of the wind vector were used by *Hirota and Niki* [1985] to extract the characteristics of its elliptical envelope and its sense of rotation. Stokes parameters [e.g., *Krauss*, 1986; *Vincent and Fritts*, 1987] later provided a framework for describing the wave ellipses that has been of great utility [e.g., *Vincent and Alexander*, 2000]. The relationships between the various forms of hodographic analysis (Stokes parameters, rotary spectra, and cross spectra) have been described by *Eckermann* [1996].

Although it was common to separate tropospheric from stratospheric parts of radiosonde profiles [*Allen and Vincent*, 1995; *Vincent et al.*, 1997], it was still possible for coincident gravity waves to be superimposed.

The potential for this to adversely affect parameter extraction was noted by *Eckermann and Hocking* [1989]. *Fritts and Alexander* [2003] also note that rotary spectral analyses are not well suited to analysis of polarized (elliptical) wind variations; an elliptically polarized upward propagating wave can be misidentified as a combination of circularly polarized upward and downward wave combinations.

An improvement to these analysis techniques that removed many of the problems noted above was provided when wavelet analysis techniques [see, e.g., *Torrence and Compo*, 1998] were applied to localize gravity waves in radiosonde profiles according to their height and vertical wavelength [*Zink and Vincent*, 2001a, 2001b]. This technique, which allows the identification of wave packets, is used here and is described more extensively in the next section.

The use of operational radiosondes makes gravity wave parameter extraction possible over a wide geographical expanse of the Earth. Maps of tropospheric and lower stratospheric wave activity over North America have been produced [*Wang and Geller*, 2003; *Wang et al.*, 2005; *Zhang et al.*, 2013] that show significant variations with season and latitude. Asian observations have included sites in China [*Zhang and Yi*, 2007], Korea [*Chun et al.*, 2007; *Ki and Chun*, 2010], India [*Leena et al.*, 2012], and Japan [*Kitamura and Hirota*, 1989; *Tateno and Sato*, 2008] that are affected by a variety of convective and dynamical processes.

Of particular interest to this study are radiosonde observations of gravity waves at middle to high southern latitudes. *Guest et al.* [2000] investigated inertia-gravity waves in the lower stratosphere near Macquarie Island (54.5°S, 159.0°E) and identified a common synoptic pattern associated with gravity wave occurrence. Using ray tracing, they were able to link this pattern to their observed waves. They also noted that downward propagating gravity waves were most common in the wintertime.

Yoshiki and Sato [2000] used radiosonde observations at 33 stations in the polar regions over 10 years (1987–1996) to contrast gravity wave activity in the northern and southern polar stratospheres. They noted that northern kinetic and potential energies in the 15–20 km height range maximize in winter, whereas in the Southern Hemisphere, they maximize in spring. Relationships to potential sources differ between the two hemispheres, and it is suggested that the polar night jet could play a role over Antarctica.

Two years of radiosonde observations from Syowa Station (69.0°S, 39.6°E) are analyzed by *Yoshiki et al.* [2004], and it is shown that the seasonal variation of wave kinetic and potential energy is dependent on height and differs from year to year. A common factor in sporadic large values of potential energy between 15 and 25 km is identified; these bursts occur when Syowa is near the edge of the polar vortex. The characteristics of these large potential energy waves are said to differ from those more commonly seen.

Sato and Yoshiki [2008] used observations from a series of 3-hourly radiosonde observing campaigns from Syowa Station to further investigate gravity wave generation near the polar vortex. Four 10 day campaigns were run at Syowa in March, June, October, and December of 2002. The frequent soundings allow frequency wave number spectra to be formed, and waves were identified for further analysis. Simultaneous upward and downward propagating waves were found, which had similar horizontal wavelengths and phase velocities. Model simulations and comparisons with measures of imbalance in the polar night jet both suggested that this could be the wave source.

The identification of the Antarctic Peninsula as a region of high stratospheric gravity wave activity and high momentum flux [*Ern et al.*, 2004; *Vincent et al.*, 2007; *Hertzog et al.*, 2008] has enhanced interest in radiosonde studies in that area. Using observations from Rothera (67.6°S, 68.1°W), *Moffat-Griffin et al.* [2011] found lower stratospheric wave energy densities peaking at the equinoxes and enhanced levels of downward wave propagation in the wintertime. *Moffat-Griffin et al.* [2013] applied a similar analysis on observations from the Falkland Islands, east of the southern tip of South America (Mount Pleasant airport, 52.8°S, 58.4°W) and found similar variations in downward wave percentages but different energy density variations.

Observations made using South Pole radiosonde soundings between 1993 and 1996 are presented by *Pfenninger et al.* [1999]. Some care is taken to ensure that the background temperature profile is correctly removed before background atmosphere and wave spectral characteristics are described. The spectral slope is found to be less than the values obtained at lower southern latitudes. Stratospheric gravity wave activity tends to be strongest in spring. Stokes parameters are used to show that downward propagating waves occur in the stratosphere approximately 20% of the year.

Table 1. Background Atmosphere and Stokes Analysis Parameters

Parameter	Description	Note/Reference
$\overline{u}$	background zonal wind	sonde background fit
$\overline{v}$	background meridional wind	sonde background fit
$\overline{u}_h$	background wind (full)	$\overline{u}_h = \sqrt{\overline{u}^2 + \overline{v}^2}$
ϕ_w	horizontal wind direction[a]	sonde background fit
$\overline{T}$	background temperature	sonde background fit
$\overline{p}$	background pressure	sonde background fit
$\overline{\rho}$	background density	from sonde parameters
z	altitude	wavelet reconstruction central altitude
λ_z	vertical wavelength	averaged around peak in z-scale space
ϕ	wave propagation direction[a]	from Stokes parameters [*Zink*, 2000]
$u_{\parallel}$	wind in propagation direction	from Stokes parameters
$v_{\perp}$	wind perpendicular to the direction of propagation	from Stokes parameters
$\hat{\omega}$	intrinsic frequency	from Stokes parameter-derived axial ratio $\hat{\omega}/f = \lvert u_{\parallel}\rvert/\lvert v_{\perp}\rvert$
N	Brunt Väisälä frequency	from background temperature profile [e.g., *Andrews et al.*, 1987]
m	vertical wave number	$m = 2\pi/\lambda_z$

[a]Degrees clockwise from north.

It is clear that a need for improved gravity wave observations exists and that operational radiosondes are making an important contribution to our knowledge of inertia-gravity wave parameters and sources. In the following section (and the appendices), the method of data analysis is described. Section 3 describes the subset of the wave spectrum visible with this analysis and the characteristics of the observed waves. The implications of these observations for source mechanisms, wave kinetic and potential energies, propagation effects, and the momentum fluxes are discussed in section 4 before drawing conclusions in the final section.

2. Data and Analysis

Data used in this study were obtained from operational radiosondes launched from Davis (68.6°S, 78.0°E) between 2001 and 2012. The instrument packages were Vaisala GPS sonde models RS80G and RS92G (changing models on 24 February 2006). The number of releases varied between one and two per day. Vertical sampling was at 2 s intervals (approximately 10 m vertical spacing), but the data were averaged to 100 m resolution to limit the influence of differing response time for the wind and temperature measurements.

Sonde wind and temperature profiles were analyzed using wavelet techniques described in *Zink and Vincent* [2001a]. Peaks were identified in wavelet power as a function of scale and altitude. Wavelet coefficients in the vicinity of the peak were used to reconstruct temperature and wind perturbations associated with each wave around the wave altitude z and to estimate the vertical wavelength λ_z. The background atmosphere states (zonal wind $\overline{u}$, meridional wind $\overline{v}$, temperature $\overline{T}$, and pressure $\overline{p}$) at the height of the wavelet were also obtained. Stokes parameters [e.g., *Krauss*, 1986] were calculated and used to obtain the wave propagation direction, the wind components of the wave parallel $u'_{\parallel}$ and perpendicular $v'_{\perp}$ to propagation, and the intrinsic frequency $\hat{\omega}$. The Brunt-Väisälä frequency N averaged over the vertical extent of the wave was obtained from the background temperature profile.

Some data rejection was applied on the basis of the Stokes parameters. Values of P (covariance between $u'_{\parallel}$ and $v'_{\perp}$) and Q (covariance between $u'_{\parallel}$ and phase-shifted $v'_{\perp}$) less than an empirically derived value of 0.05 $m^2\ s^{-2}$ were taken as an indication of weak wave activity and were rejected. Values of depolarization greater than 1 were found and were also rejected; if the assumptions of the Stokes analysis are satisfied, such depolarization values should not occur so they were taken as an indicator of unsatisfied assumptions. A possible cause is having partial wave cycles present in the data. Data were also vetted for the relative phase between $u'_{\parallel}$ and temperature T'. Those values were within a 10° range centered on 0° or 180°; the values were removed. This is a similar constraint to that used in *Moffat-Griffin et al.* [2011].

As noted above, there were potential problems with some analysis methods previously used [*Eckermann and Hocking*, 1989; *Fritts and Alexander*, 2003]. The wavelet analysis used here mitigates these. By separating waves into individual events, it also allows for the extraction of combinations of parameters for each wave

Table 2. Intrinsic Parameters

Parameter	Description	Note/Reference
k_h	horizontal wave number (full)	$k_h^2 = \frac{f^2 m^2}{N^2}\left(\frac{\hat{\omega}^2}{f^2} - 1\right)$ [after *Fritts and Alexander*, 2003, equation (38)]
λ_h	horizontal wavelength	$\lambda_h = 2\pi/k_h$
k	zonal wave number	$k = k_h \sin\phi$
l	meridional wave number	$l = k_h \cos\phi$
$\hat{c}_z$	intrinsic vertical phase speed	$\hat{c}_z = \hat{\omega}/m$ [e.g., *Lighthill*, 1978]
$\hat{c}$	intrinsic horizontal phase speed	$\hat{c} = \hat{\omega}/k_h$
$\hat{c}_x$	intrinsic zonal phase speed	$\hat{c}_x = \hat{\omega}/k$
$\hat{c}_y$	intrinsic meridional phase speed	$\hat{c}_y = \hat{\omega}/l$
$\hat{c}_{gz}$	intrinsic vertical group velocity	$\hat{c}_{gz} = -\frac{1}{\hat{\omega}m}(\hat{\omega}^2 - f^2)$ [after *Fritts and Alexander*, 2003, equation (38)]
$\hat{c}_{gx}$	intrinsic zonal group velocity	$\hat{c}_{gx} = \frac{kN^2}{\hat{\omega}m^2}$ [after *Fritts and Alexander*, 2003, equation (38)]
$\hat{c}_{gy}$	intrinsic meridional group velocity	$\hat{c}_{gy} = \frac{lN^2}{\hat{\omega}m^2}$ [after *Fritts and Alexander*, 2003, equation (38)]
$\hat{c}_{gh}$	intrinsic horizontal group velocity	$\hat{c}_{gh} = \sqrt{\hat{c}_{gx}^2 + \hat{c}_{gy}^2}$ in direction of wave propagation

packet and the compilation of statistics of those parameters. These statistics will provide a focus for the analysis used here.

3. Results

The wavelet technique described in the previous section provides direct estimates of wind and temperature perturbation amplitudes, vertical wavelength and other gravity wave and background atmosphere parameters, and through the polarization relation for low-frequency gravity waves, the intrinsic frequency $\hat{\omega}$ (see Table 1). These gravity wave characteristics are thus determined with few assumptions. The low-frequency version of the dispersion relation [*Fritts and Alexander*, 2003] and various wave parameter relations [e.g., *Lighthill*, 1978] allow other gravity wave parameters to be estimated as described in Table 2.

3.1. Gravity Wave Sampling

Alexander [1998] noted that each observing technique has its own "observational filter." Of interest in this context are the vertical and horizontal wavelengths and intrinsic frequency of the observed waves [after *Hertzog et al.*, 2008]. These parameters have been calculated for each wave packet and are shown in Figure 1; upward and downward propagating waves are shown in red and blue, respectively. Figure 1a shows that

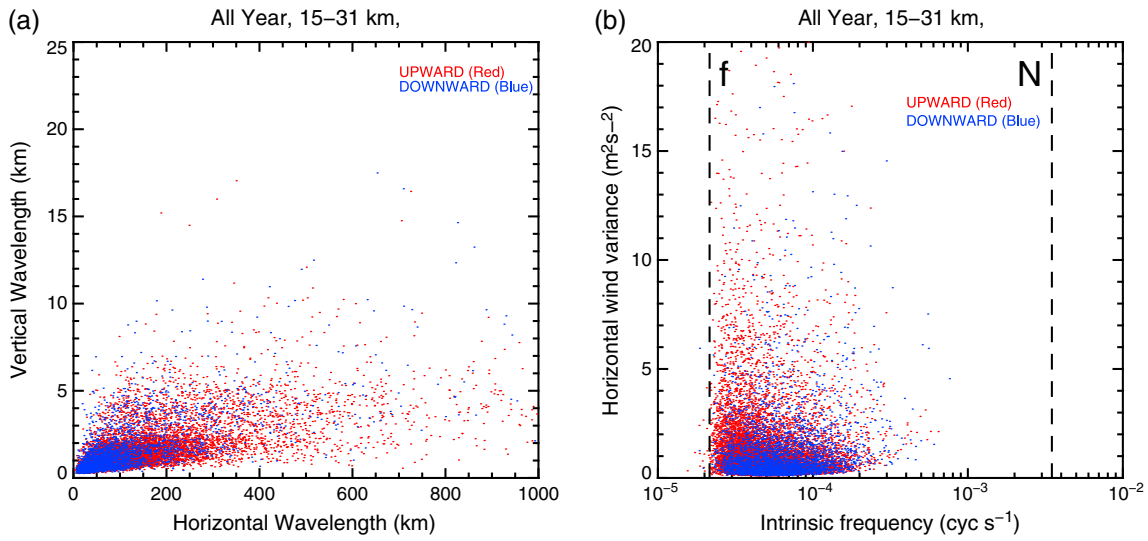

Figure 1. (a) Vertical and horizontal wavelengths for upward and downward propagating waves between 15 and 31 km. (b) Corresponding wave intrinsic frequencies and horizontal variances.

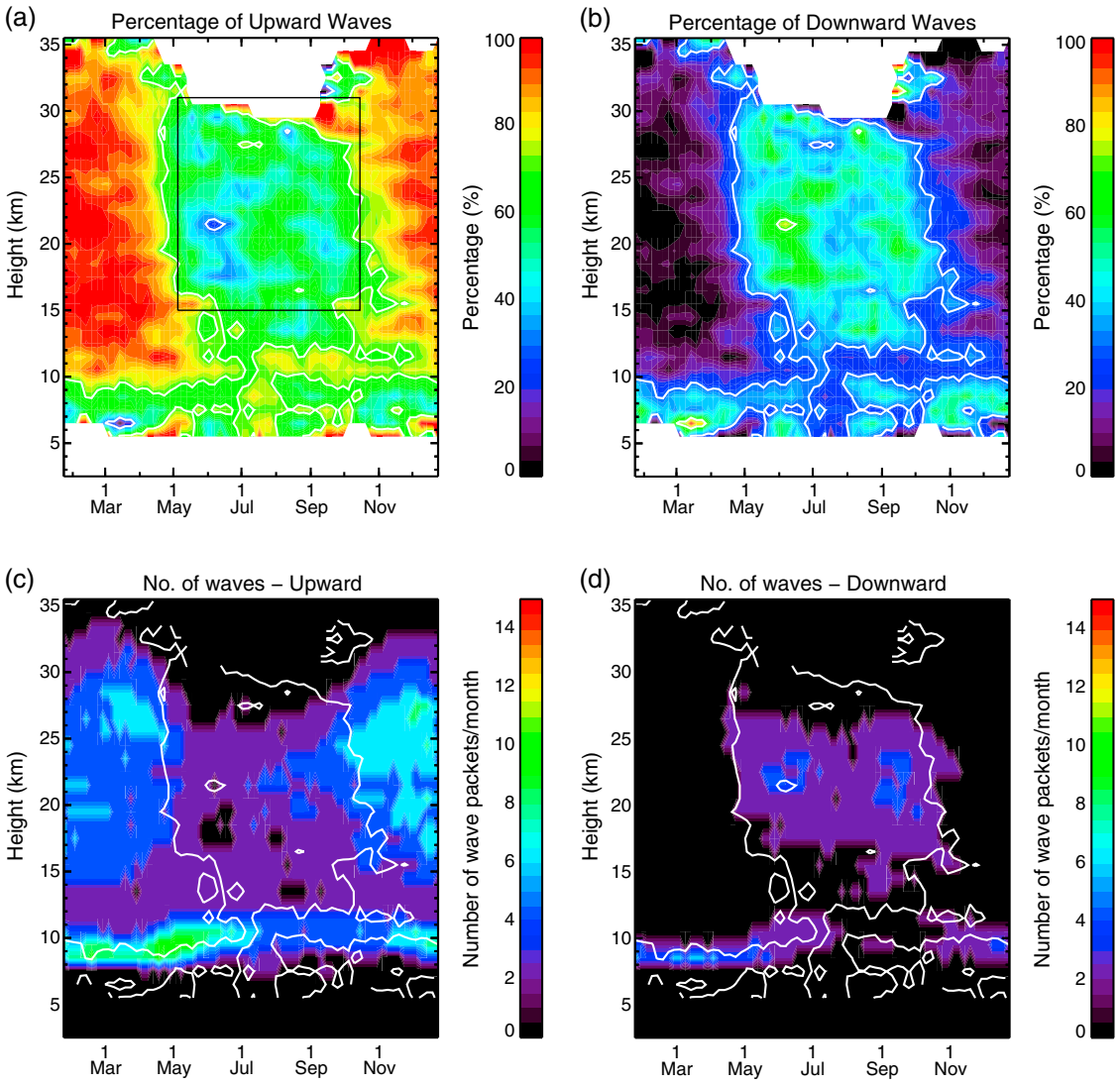

Figure 2. Seasonal variation in the percentage of (a) upward and (b) downward propagating gravity waves along with the number of (c) upgoing and (d) downgoing waves per month. Note the vertical bin size is 1 km. White contour lines are presented in all figures for 30% and 70% upward or downward waves. The box overlying Figure 2a is used to accumulate winter half year statistics of wave parameters.

most vertical wavelengths fall below 2–3 km (median value is 1 km). The use of a mother Morlet wavelet that contains approximately five cycles in its Gaussian envelope [*Zink and Vincent*, 2001a] limits the maximum vertical wavelength observable; waves whose vertical wavelength is greater than approximately one fifth of the vertical observing range will not project strongly onto the mother wavelet. Thus, the upper limit of the observed vertical wavelength is likely an observational filter effect associated with the chosen wavelet characteristics.

Figure 1b shows that low values of intrinsic frequency (periods near the inertial period $1/f$ of 12.9 h at Davis) are most common for this observing technique. Approximations to the full dispersion relation [*Fritts and Alexander*, 2003] show that the intrinsic frequency has a proportional relationship to the vertical wavelength. The prevalence of low-frequency waves may thus be a consequence of the filtering in vertical wavelength described above. Comparison of Figure 1 to Antarctic stratosphere superpressure balloon results in *Hertzog et al.* [2008] show that the range of observed intrinsic frequencies is similar but that their technique sees a greater population of vertical wavelengths larger than the values shown here.

The median value of intrinsic frequency corresponds to a period of approximately 5 h. At its vertical ascent rate (~5 ms^{-1}), the balloon will transit the stratospheric sampling region in approximately an hour

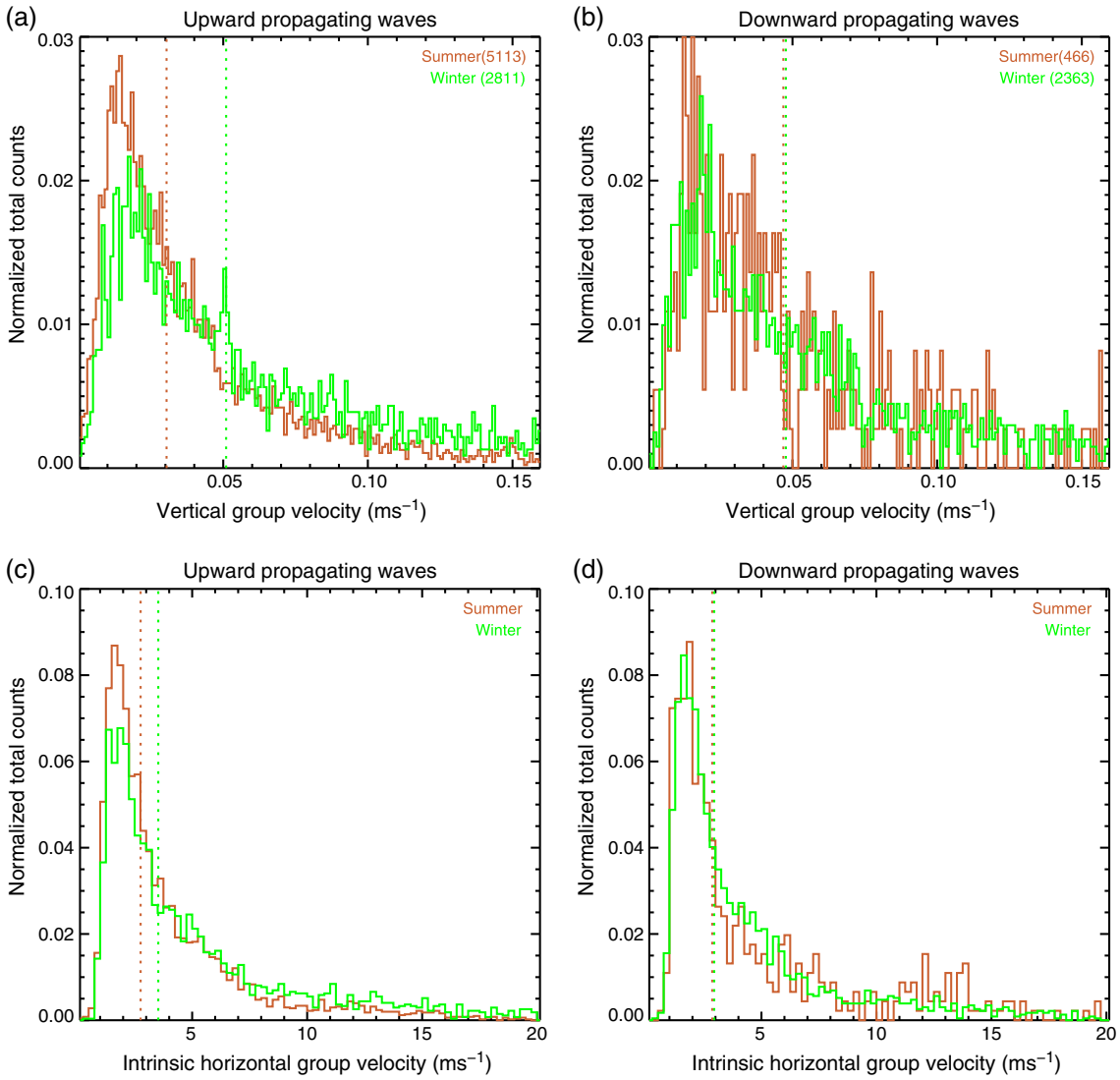

Figure 3. Distributions of the vertical group velocity for (a) upward and (b) downward propagating waves and (c and d) intrinsic horizontal group speed in the summer and winter half years. Distributions are normalized by total counts. Median values are marked with a vertical line.

and the vertical extent of the wave packet in a shorter time. Thus, these waves are sampled relatively instantaneously (compared to their rate of change) by the radiosonde.

3.2. Vertical Propagation Direction and Speed

The vertical propagation direction is derived from the sense of rotation with altitude of the head of the wind vector, which is described by the Stokes parameter Q (see Appendix A): positive for anticlockwise and negative for clockwise rotation [*Eckermann and Vincent*, 1989]. In the Southern Hemisphere (where the Coriolis parameter f is negative), Q is negative for upward propagating waves and positive for downward waves [*Hirota and Niki*, 1985; *Moffat-Griffin et al.*, 2011].

The 12 year average seasonal variation in the number of upward and downward propagating waves, expressed as both a percentage and the number of waves per month, is given in Figure 2. Note that small values of Q were rejected to help prevent incorrect assignment of propagation direction. A high percentage of downward propagating waves is apparent from May to October above approximately 13 km. White contour lines at 30% and 70% show the form of the enhanced downward propagation feature. Figures 2c and 2d show that the increase in downward propagating waves largely coincides with a decrease in upward waves, i.e., the downward waves tend to be replacement rather than additional

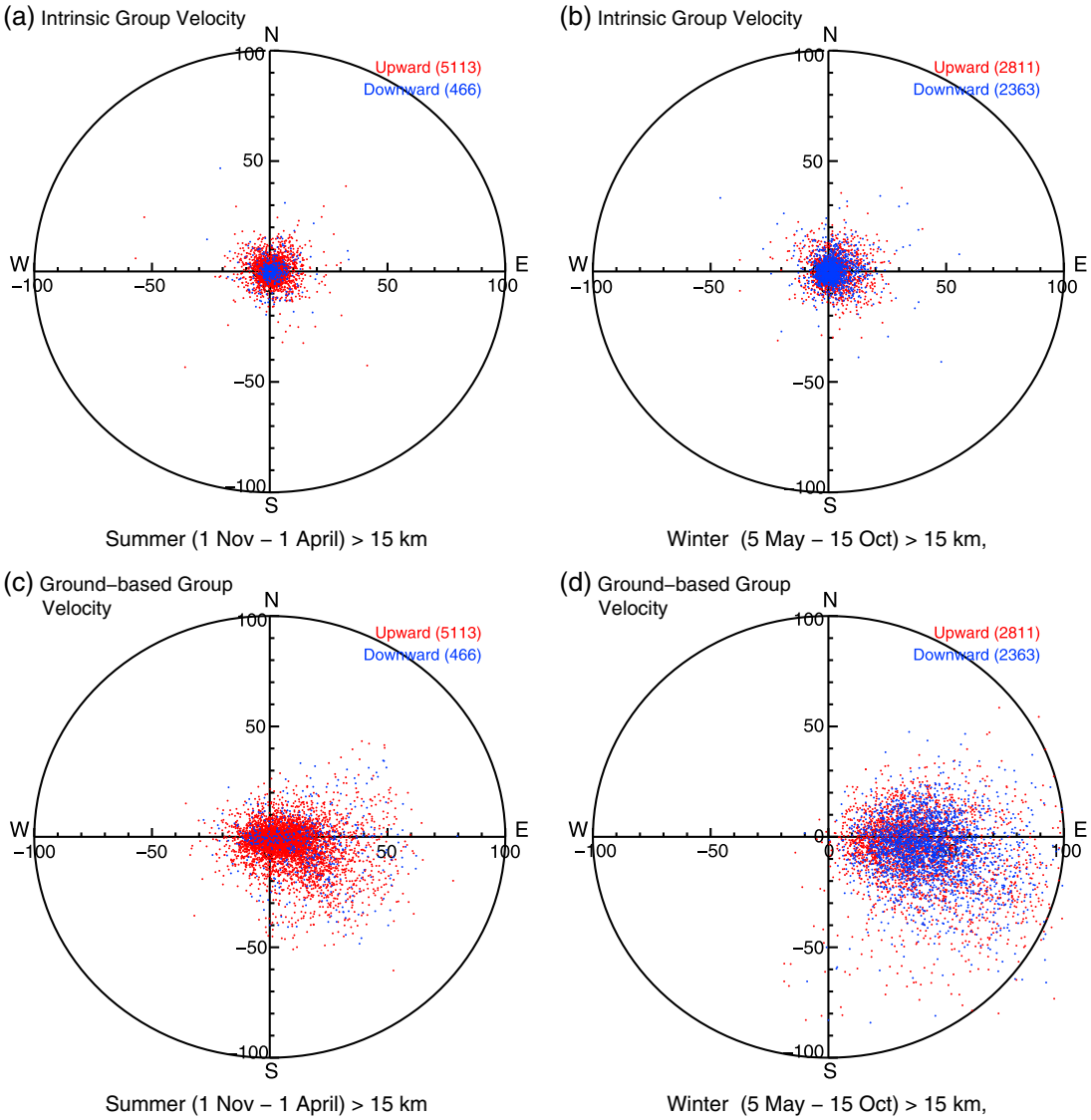

Figure 4. Polar plots of the horizontal group velocity (in m s^{-1}) for (a and c) summer and (b and d) winter intervals in the intrinsic (Figures 4a and 4b) and ground-based (Figures 4c and 4d) frames. Upward (downward) waves are indicated in red (blue).

waves. The increased number of downward waves was noted by *Moffat-Griffin et al.* [2011] for the Antarctic Peninsula station at Rothera (67°S, 68°W) over a similar interval. Other authors have also identified downward propagating gravity waves in the southern polar stratosphere [*Guest et al.*, 2000; *Yoshiki and Sato*, 2000; *Zink and Vincent*, 2001a; *Yoshiki et al.*, 2004; *Sato and Yoshiki*, 2008]. The vertical structure seen here shows that downward propagating waves occur over a wide range of heights and that the increase and decrease in the number of downgoing waves do not occur simultaneously at all the observed heights.

The change in the character of the stratospheric gravity wave field that occurs in early May and mid-October suggests natural groupings for the compilation of statistics. These approximately half-year intervals are denoted summer (1 November to 1 April) and winter (5 May to 15 October). The distribution of half-yearly vertical group velocities c_{gz} for upward and downward propagating waves are given in Figures 3a and 3b. Median values are shown using a vertical line and have low values (0.05 m s^{-1} ≈4.3 km d^{-1}. Summer-winter differences in median c_{gz} in the upward propagating waves are larger than for the downward waves. The forms of the distributions are similar in all cases.

Table 3. Ground-Based Parameters

Parameter	Description	Note/Reference
c_{gx}	zonal group velocity	$c_{gx} = \hat{c}_{gx} + \overline{u}$ [after *Fritts and Alexander*, 2003, equation (25)]
c_{gy}	meridional group velocity	$c_{gy} = \hat{c}_{gy} + \overline{v}$ [after *Fritts and Alexander*, 2003, equation (25)]
c_{gz}	vertical group velocity	$c_{gz} = \hat{c}_{gz}$
ω	ground-based frequency	$\omega = \hat{\omega} + \lvert k_h \rvert \lvert \overline{u}_h \rvert \cos(\phi_w - \phi)$
c_x	zonal phase velocity	$c_x = \hat{c}_x + \overline{u} + \overline{v}l/k$
c_y	meridional phase velocity	$c_y = \hat{c}_y + \overline{u}k/l + \overline{v}$
c	phase velocity	$c = \hat{\omega}/k_h + \overline{u}_h \cos(\phi_w - \phi)$
$\overline{u'w'}$[b]	zonal momentum flux	$\overline{u'w'} = -\frac{\rho\hat{\omega}}{N^2} g \overline{u' \frac{T'_{+90}}{\overline{T}}}$ [*Zink and Vincent*, 2001b]
$\overline{v'w'}$[b]	meridional momentum flux	$\overline{v'w'} = -\frac{\rho\hat{\omega}}{N^2} g \overline{v' \frac{T'_{+90}}{\overline{T}}}$ [*Zink and Vincent*, 2001b]
KE[b]	kinetic energy	$\mathrm{KE} = \frac{1}{2}\left[\overline{u'^2} + \overline{v'^2}\right]$
PE[b]	potential energy	$\mathrm{PE} = \frac{g^2}{2N^2}\overline{\frac{T'^2}{\overline{T}}}$

[b]Overbar indicates average of wave packet.

3.3. Horizontal Propagation Direction and Speed

Intrinsic horizontal group velocities (i.e., those measured in the frame of the background wind at the point of measurement) for the summer and winter intervals are presented in Figures 3c and 3d and are somewhat faster than the vertical group velocities. This is consistent with the idea that these waves have shallow propagation angles [*Fritts and Alexander*, 2003] and that they can propagate large distances during their life cycles [*Tateno and Sato*, 2008]. Once again, there are strong similarities between the distributions of upward and downward propagating waves with winter median horizontal group velocities both being close to 3 m s^{-1}.

The nature of wave propagation above Davis changes dramatically between summer and winter due to the strong background winds associated with the stratospheric polar vortex. Figures 4a and 4b show the summer and winter gravity wave intrinsic group velocities in polar form. It can be seen that the distribution is centered near zero in both cases. However, the same velocities transformed into the ground-based frame (as described in Table 3) shown in Figures 4c and 4d are significantly altered by the background wind and in the case of the winter, dramatically so. It is clear from Figure 4d that the propagation of the observed waves in the ground-based frame is dominated in winter by advection of the wave; the waves are being blown along by the background wind more strongly than they are propagating relative to the wind. *Sato et al.* [2012] describe the propagation geometry of a stationary gravity wave and note that the direction of propagation in the ground-based frame can differ from that in the intrinsic frame. The observations presented here demonstrate a similar effect but for nonstationary waves.

As noted above, radiosondes sample the waves relatively instantaneously. The median values of vertical group velocity shown in Figure 3 range between 0.03 and 0.05 m s^{-1}, which equate to multiday transit times for the vertical span of our observations. The ground-based velocities depicted in Figures 4c and 4d suggest that even for wave lifetimes of a few cycles, the waves travel large distances horizontally. Our observations, therefore, will capture fewer examples of source or dissipation processes of the waves; the distribution in Figure 3 will largely contain contributions from times within the waves' life cycle (although source and dissipation observations are not precluded).

The character of the observed gravity waves during the wintertime, in particular the large percentage of downward propagating waves, is of interest because upward propagating gravity waves are considered most common in the stratosphere away from the southern polar regions [*Yoshiki and Sato*, 2000]. For the remainder of this paper, there is an emphasis on stratospheric gravity waves observed in winter.

3.4. Characteristics of Wintertime Waves

Distributions of the available gravity wave characteristics (described in Tables 1–3) are compiled within the interval 5 May to 15 October (hereafter termed winter) and the height range 15–31 km. Observations above

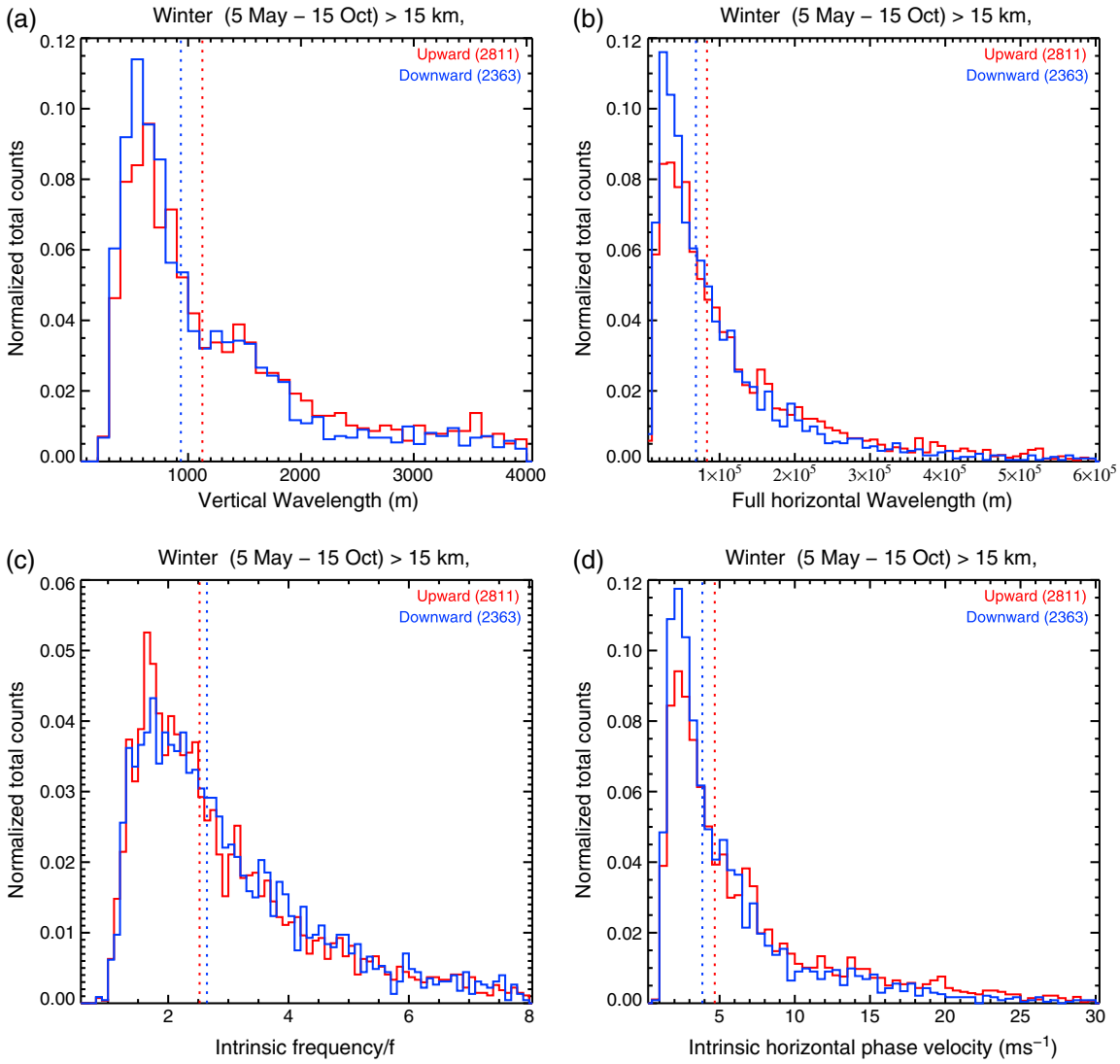

Figure 5. Distributions (normalized by total counts) of wintertime (5 May to 15 October) (a) vertical wavelength λ_z, (b) full horizontal wavelength λ_h, (c) intrinsic frequency $\hat{\omega}$ (in units of f), and (d) intrinsic horizontal phase velocity $\hat{c}$ magnitude. Upward (downward) waves are indicated in red (blue). Dashed lines indicate the median.

this range are not available throughout the year and are excluded. Below 15 km, effects of the removal of the background temperature variations around the tropopause could adversely affect the parameter extraction.

Distributions of vertical and horizontal wavelength (λ_z, λ_h), intrinsic frequency ($\hat{\omega}$), and intrinsic phase velocity ($\hat{c}$) are presented in Figure 5. For these and all other calculated wave characteristics (with the exception of propagation direction), the wintertime distributions of upward and downward propagating waves are similar. Inspection of the distributions of vertical and horizontal wavelength and intrinsic frequency during June–August presented by *Yoshiki et al.* [2004] show a similar consistency between upward and downward propagating waves above Syowa.

4. Discussion

4.1. Source Model

Studies of gravity wave sources reflect a focus on the troposphere as the key gravity wave production region [*Fritts and Alexander*, 2003; *Alexander et al.*, 2010]. The high percentage of wintertime downward propagating waves shown in Figure 2 cannot be explained with a troposphere-only source. The simple addition of a stratospheric source that creates the waves seen propagating downward is problematic due to the

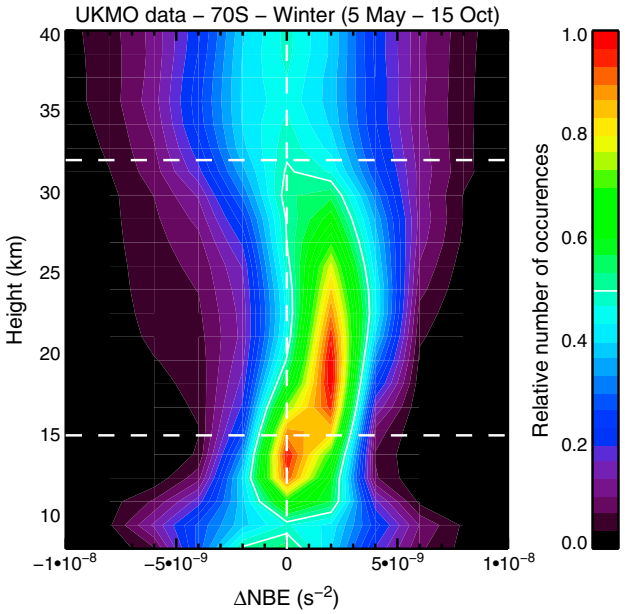

Figure 6. Stacked histograms versus height (normalized by maximum occurrence rate) of wintertime (5 May to 15 October) UKMO-assimilated data nonlinear balance equation residual (ΔNBE) on the longitude circle at 70°S versus height. The 50% occurrence rate has been contoured. Horizontal lines indicate the vertical range 15 to 32 km.

similarity of the characteristics of the upgoing and downgoing waves (see Figure 5); the additional stratospheric source would need to replicate the tropospheric one. A simpler explanation for this similarity is a common source mechanism for waves propagating upward and downward.

Production of such wave combinations is not without precedent. Using radar winds, *Thomas et al.* [1999] identified upward and downward propagating gravity waves in the vicinity of a jet stream near the upper tropopause. *Plougonven et al.* [2003] and *Zhang and Yi* [2007] similarly identified upward and downward waves using midlatitude radiosonde observations. Case studies by *Sato and Yoshiki* [2008] identify upgoing and downgoing waves in the polar stratosphere whose similarity suggests a common source. They then consider the possibility of spontaneous generation in the polar night jet by investigating measures of departure from geostrophic balance. *Pfenninger et al.* [1999] note a lack of correlation between tropospheric and stratospheric wave characteristics and suggest sources for the observed waves in each region.

If a common source mechanism for upgoing and downgoing waves is to be invoked here, then it needs to be distributed across the observed region of combined upward and downward propagating waves to explain both wave populations. A variety of measures can be used to assess this possibility, including the Rossby number, which can be defined in its Lagrangian form as the ratio of relative vorticity ζ to planetary vorticity $Ro = \zeta/f$ [*Pedlosky*, 2003; *Sato and Yoshiki*, 2008] or in its cross-stream Lagrangian form $|\mathbf{V}_{ag}^{\perp}|/|\mathbf{V}|$ where $\mathbf{V}_{ag}^{\perp}$ is the ageostrophic wind component perpendicular to the wind $\mathbf{V}$ [*Koch and Dorian*, 1988; *Tateno and Sato*, 2008]. These measures are summarized in *Plougonven and Zhang* [2013] along with the residual of the nonlinear balance equation, ΔNBE, defined as

$$\Delta\mathrm{NBE} = 2J(u,v) + f\zeta - \nabla^2\Phi - \beta u, \tag{1}$$

where $J(u,v)$ is the Jacobian of u and v, Φ is the geopotential height, and $\beta = \partial f/\partial y$ is the meridional gradient of the Coriolis parameter [see *Zhang*, 2004]. Of these three, ΔNBE is considered the more sophisticated measure of imbalance and will be used here.

Histograms of ΔNBE for each height compiled using UK Met Office (UKMO)-assimilated data [*Swinbank et al.*, 2006] at all longitudes and 70°S for the winter interval defined previously are shown in Figure 6. The vertical distribution of nonlinear balance residual has a strong tendency to be positive during the winter interval. This suggests that the imbalance processes could be occurring throughout the height region of our observations.

The timing of variations in nonlinear balance residual is shown in Figure 7 where average values over Davis from 2004 to 2012 are presented. Inspection of the contours, which describe downgoing wave percentages of 30% and 70% (see Figure 2), shows a strong similarity to ΔNBE. The upper limit of the percentage occurrence contour falls close to the upper limit of the data (around 30 km in winter); it is not clear if downward propagating waves continue to occur above our observations, so conclusions cannot be drawn about a relationship at this upper boundary.

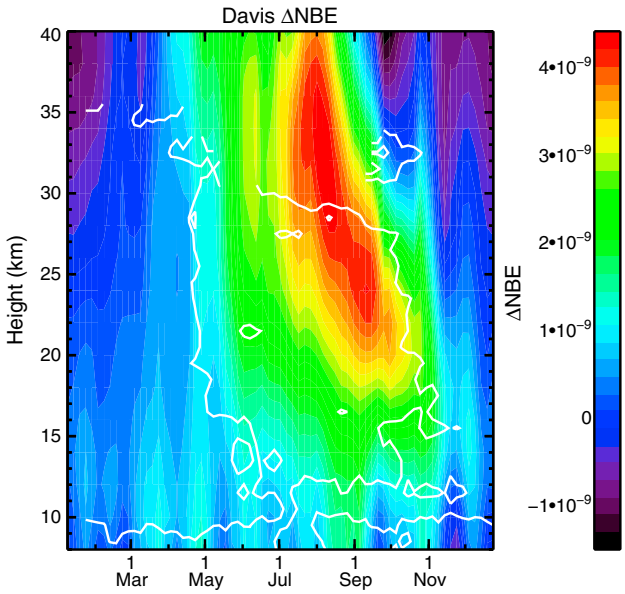

Figure 7. Seasonal variation of average nonlinear balance equation residual (ΔNBE) above Davis. White contour lines of 30% and 70% upward or downward waves are superimposed.

The use here of the *average* value of ΔNBE may not be ideal; imbalance likely occurs when a threshold value is achieved and the number exceeding a threshold may not follow the mean. The normalization used in Figure 6, which factors against the maximum occurrence rate for all heights, demonstrates a broadening of the distribution with increasing height (the distribution narrowing between 14 and 20 km). It would be more appropriate to indicate the rate at which the imbalance threshold is exceeded. However, as noted in *Plougonven and Zhang* [2013], such quantitative measures are not trivial.

Zhang [2004] applies the nonlinear balance residual to a modeled flow through a criterion that states that the system is unbalanced if the amplitude of any one of the terms in (1) is greater than the residual itself. Figure 8 shows a latitude-longitude cross section of the nonlinear balance residual, along with the terms contributing to it. The field presented is that for a height of 20 km (but that near 30 km is similar) with Davis being used as the reference location for height calculations (indicated by a square). It can be seen that the nonlinear residual is dominated by the $f\zeta$ term. Noting that $\zeta = \partial v/\partial x - \partial u/\partial y$, it is clear that the latter term will become large in the vicinity of the meridional shear of zonal wind associated with the polar vortex. This is supported by the composite of the wind structure contoured in Figure 8b. The dominance of this term means that the nonlinear balance residual term is almost always of larger magnitude than the terms displayed in Figures 8c–8e. This is found to be true throughout the year at these heights, not just in winter. Thus, the criterion suggested by *Zhang* [2004] is always met and cannot be used effectively here.

The horizontal resolution of the UKMO-assimilated data used here [*Swinbank et al.*, 2006] is less than that of the numerical simulations performed by *Zhang* [2004]. The fine-scale structure resolved in their study that could suggest imbalance would not be resolved here. Thus, the nonlinear balance residuals calculated in this study (and the magnitude of the shears contributing to them) would be conservative compared to those in *Zhang* [2004].

It is noted that the second term of the nonlinear balance residual equation, $f\zeta$, and the Rossby number, ζ/f, are proportional to each other at a given latitude. Examination of the Lagrangian Rossby number (not shown) gives very similar results to those shown here due to the dominance of the vorticity term in (1) at our heights and latitude.

A scale analysis of the physics underlying the derivation of (1) was carried out by *Plougonven and Zhang* [2007], and it was shown that the nonlinear balance residual by itself was not sufficient as a diagnostic for gravity wave forcing; in their study, the Lagrangian derivative of its vertical gradient appears as an important term.

The analysis carried out by *Zhang* [2004] is for a low-latitude site. High-latitude stratospheric sites such as the one considered in this paper have higher values of f, zonal wind, and meridional shear in zonal wind. Although defining a threshold for gravity wave production is beyond the scope of this paper, these latitudinal factors would need to be taken into account if it is to be used at high latitudes. However, the similarity between downward propagating wave percentages and ΔNBE shown in Figure 7 suggests a role for imbalance in gravity wave production and supports the concept of a source of gravity waves vertically distributed across the southern polar lower stratosphere.

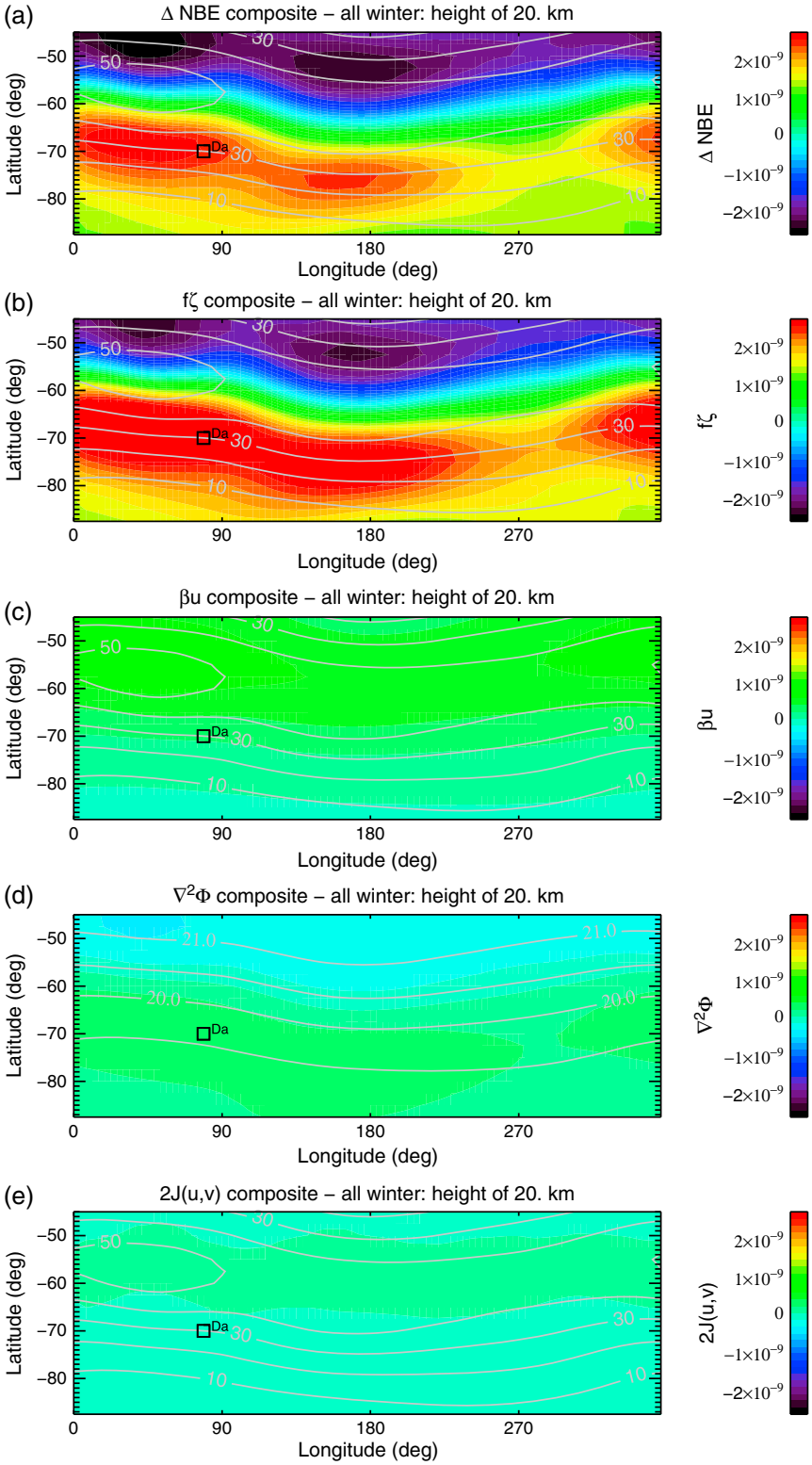

Figure 8. (a–e) Latitude-longitude section of the wintertime nonlinear balance equation residual at 20 km and the terms contributing to it. Contours are of background zonal wind (in m s^{-1}) with the exception of Figure 8d which contours geopotential height. The position of Davis is indicated.

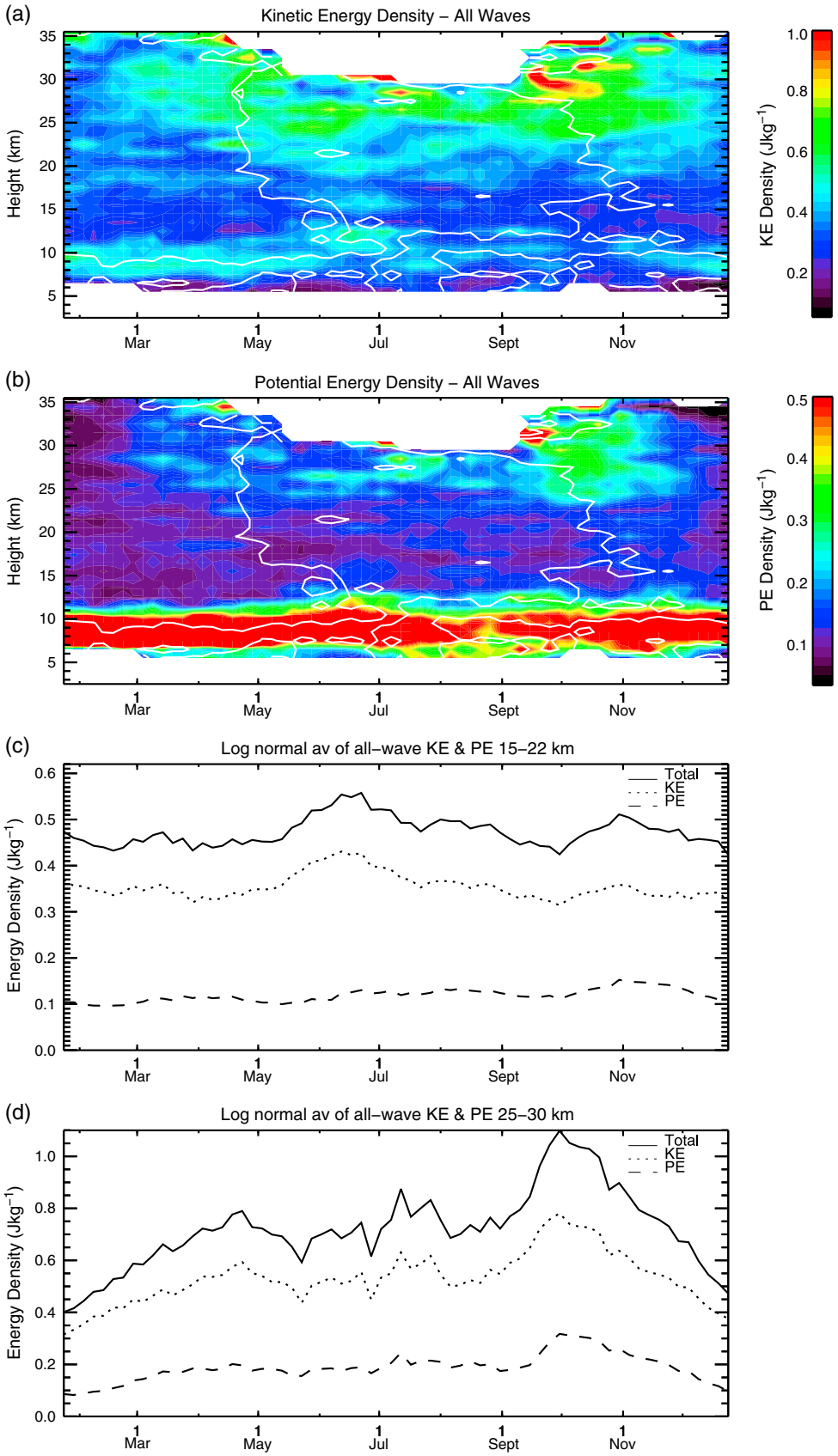

Figure 9

4.2. Kinetic and Potential Energy

The total energy carried by the observed waves can be calculated using the equation

$$E_0 = \frac{1}{2}\left[\overline{u'^2} + \overline{v'^2} + \frac{g^2\overline{\hat{T}'^2}}{N^2}\right], \quad (2)$$

where $\hat{T}' = T'/\langle T\rangle$ is the wave temperature perturbation divided by the background temperature and the overbar indicates an average over the vertical span of the wave [*Vincent et al.*, 1997]. Vertical velocity perturbations have been assumed to be small and are not included in this equation. The velocity terms describe the kinetic energy density, whereas the temperature term describes the potential energy density.

Kinetic and potential energy densities of the observed wave packets, averaged using lognormal statistics as described in *Baumgaertner and McDonald* [2007], are presented in Figure 9. Figures 9a and 9b show the variation of these quantities as a function of height and season. Both potential and kinetic energies are larger above 22 km and show a strong seasonal variation at the upper heights. This seasonal variation is similar in form (but not magnitude) to that shown by *Yoshiki and Sato* [2000] and *Yoshiki et al.* [2004] for Syowa Station, which is at the same latitude but 40° to the west of Davis. A peak in potential energy between October and December seen by *Yoshiki and Sato* [2000] and by *Pfenninger et al.* [1999] at South Pole is also apparent here. The white contours overlaid in Figures 9a and 9b show the 30% and 70% boundaries in vertical propagation statistics (see Figure 2); a relationship between energy density and vertical propagation is not apparent.

Line plots of the height-averaged kinetic and potential energies in the height ranges of 15–22 km and 25–30 km are shown in Figures 9c and 9d. The total energy (solid line) is dominated by the kinetic energy (dotted line) while the potential energy contribution is relatively small. This is consistent with the characteristics of the inertial gravity waves that are preferentially observed in this study (see Figures 1 and 5). The seasonal variation is stronger in the upper height range with a peak occurring in total energy density between September and November.

It is useful to compare these results to other observations, but it should be noted that a variety of analysis methods have been used. Calculated energy densities are averaged using both lognormal and linear statistics, perturbations are extracted with both wavelet and simple variance methods, and prefiltering of the vertical profile, which can affect the passband of the vertical wavelengths contributing to the energy densities, are not always the same.

In the analysis applied here, individual wave packets are isolated in vertical wavelength-altitude space when large variances are identified in the wavelet power of the wind data. The same wavelet characteristics are then used to filter the temperature; however, the temperature variance is not constrained by the analysis; it will be coherent with the wind but can be small. This analysis will (with the aid of appropriate scaling factors [see, *Zink and Vincent*, 2001a]) separate variance contributions into individual wavelets of finite vertical extent and (vertical wave number) bandwidth. Thus, it will act to band-pass filter the data and reject some contributions to the variance.

The above technique differs to that applied in the energy density studies of *Pfenninger et al.* [1999], *Yoshiki and Sato* [2000], *Yoshiki et al.* [2004], *Innis et al.* [2004], *Sato and Yoshiki* [2008], and *Moffat-Griffin et al.* [2011, 2013]. These authors calculate wind and temperature variances over height segments of the perturbation profiles. Lognormal averaging was applied in the studies by *Moffat-Griffin et al.* [2011, 2013], with the effect of decreasing the emphasis on large values. It is clear from observations [see, e.g., *Sato and Yoshiki*, 2008] that bursts of large kinetic and potential energy density can occur. *Baumgaertner and McDonald* [2007] show that the distributions of potential energy are lognormal. It is therefore prudent to use lognormal statistics (while tracking the consequences of its use when comparing results). Based on the distributions compiled for Davis, the use of lognormal averaging decreases the estimate of the mean kinetic and potential energy density by approximately a factor of 2.

Figure 9. Seasonal variation of (a) kinetic and (b) potential energy density, averaged using lognormal statistics, for all observed waves. Averages over the height range (c) 15–22 km and (d) 25–30 km of total energy (solid), kinetic energy (dotted), and potential energy (dashed) densities are also presented.

An analysis of energy densities from Antarctic radiosonde observations made between 1999 and 2002 was carried out by *Innis et al.* [2004]. Seasonal variations in the Davis (conventionally) averaged potential and kinetic energy density over the height range 13–20 km peak near 0.7 J kg^{-1} and 3.5 J kg^{-1}, respectively. Note that in *Innis et al.* [2004], the sonde vertical resolution was approximately 10 m. Both energy density values are larger than the results shown in Figure 9 for the same site and data source, illustrating the role different analysis techniques can play.

Syowa observations described by *Sato and Yoshiki* [2008] yield potential energies between 0.4 and 1.0 but up to 3.0 J kg^{-1} for the 2–8 km vertical wavelength band and between 15 and 25 km altitude. These are consistent with those in *Yoshiki et al.* [2004], but larger values are present in *Yoshiki and Sato* [2000] (even accounting for the omission of the $\frac{1}{2}$ factor in the latter). *Pfenninger et al.* [1999] present South Pole potential energy densities between approximately 0.5 and 1.5 J kg^{-1} in the 15–25 km altitude range. None of these studies use lognormal averaging, but they are broadly consistent with *Innis et al.* [2004].

Observations made at Rothera and the Falkland Islands [*Moffat-Griffin et al.*, 2011, 2013] yield potential energy density values in the 15–22 km altitude range of ≈ 0.2–0.6 J kg^{-1} and 0.5 J kg^{-1}, respectively. Noting their use of lognormal statistics, their results are similar to those at other stations. Similar comparisons using kinetic energy show broad similarity within the bounds of the differing techniques that were used, although South Pole kinetic energy values were generally larger in the wintertime [*Pfenninger et al.*, 1999].

The use of wavelet techniques to isolate the kinetic and potential energies associated with individual wave packets has the effect of decreasing energy density estimates: variance not associated with a wave packet (such as that due to subwavelet-scale variations) no longer makes a contribution. Temperature and wind are subject to different constraints in the wavelet analysis and so are affected differently. It is found that the decrease is greatest in the potential energy. However, in doing so, the contamination of the energy estimates by out-of-band waves is reduced, leading to an improved estimate of the energy density of the wave classes being considered.

4.3. Vertical Propagation Conditions

The influence that the background environment has on gravity wave propagation can be assessed by considering the relationship between the wind and atmospheric stability and wave parameters. In particular, variations in the vertical wave number m provide an indicator of vertical propagation conditions. *Tateno and Sato* [2008] note that for inertial gravity waves, the rate of change of the vertical wave number following a ray is equal to

$$\frac{d_g m}{dt} = -\frac{(k^2 + l^2)(N^2)_z}{2\hat{\omega}(k^2 + l^2 + m^2)} - k\overline{u}_z - l\overline{v}_z \tag{3}$$

where d_g/dt denotes differentiation following the group velocity of a wave and the subscript z denotes vertical gradient. It is clear from this equation that vertical propagation depends on vertical shears in horizontal wind $(\overline{u}, \overline{v})$ and on the vertical gradient of N^2.

Climatological averages of these terms, obtained from UKMO reanalysis data [*Swinbank et al.*, 2006] over the interval 2004–2012, are presented in Figures 10a, 10c, and 10e. The 30 and 70% upward and downward propagation contours are overlaid for comparison. (The vertical extent of the reanalysis data is greater than the sonde data: lack of contours above 30 km is due to a lack of observations.) Positive shears of approximately 2 m s^{-1} km^{-1} are present in the zonal winds above 10–15 km between April and November, with larger values from August to October. Weaker shears are present in the meridional wind, peaking during September–October. A vertical gradient feature is apparent in N^2 from July to November between 15 and 26 km. There is clearly a potential for changes in vertical propagation with season and height.

The vertical wave number tendency following the wave ($d_g m/dt$ scaled to units of m^{-1} d^{-1}) due to N_z^2 and $\overline{u}_z$ effects for a wave with $k = 1/80{,}000$ m^{-1}, $m = 1/1000$ m^{-1}, and $\hat{\omega} = 2.5 f_{\text{Davis}}$ is presented in Figure 10b. (Meridional influences are precluded here by setting $l = 0$.) These values of zonal wave number, vertical wave number, and intrinsic frequency approximate the medians shown in Figure 5. Note that the winter ground-based zonal phase velocities are typically positive due to the strong winds present in the winter polar stratosphere above Davis. Throughout most of the winter stratosphere, the vertical wave number tendency is negative. Thus, the vertical wave number of upgoing waves, which must be less than zero, will become *more* negative. The associated decrease in intrinsic frequency (see equation (B1)) implies a potential for critical level encounters. Such encounters cannot be identified explicitly with these data because

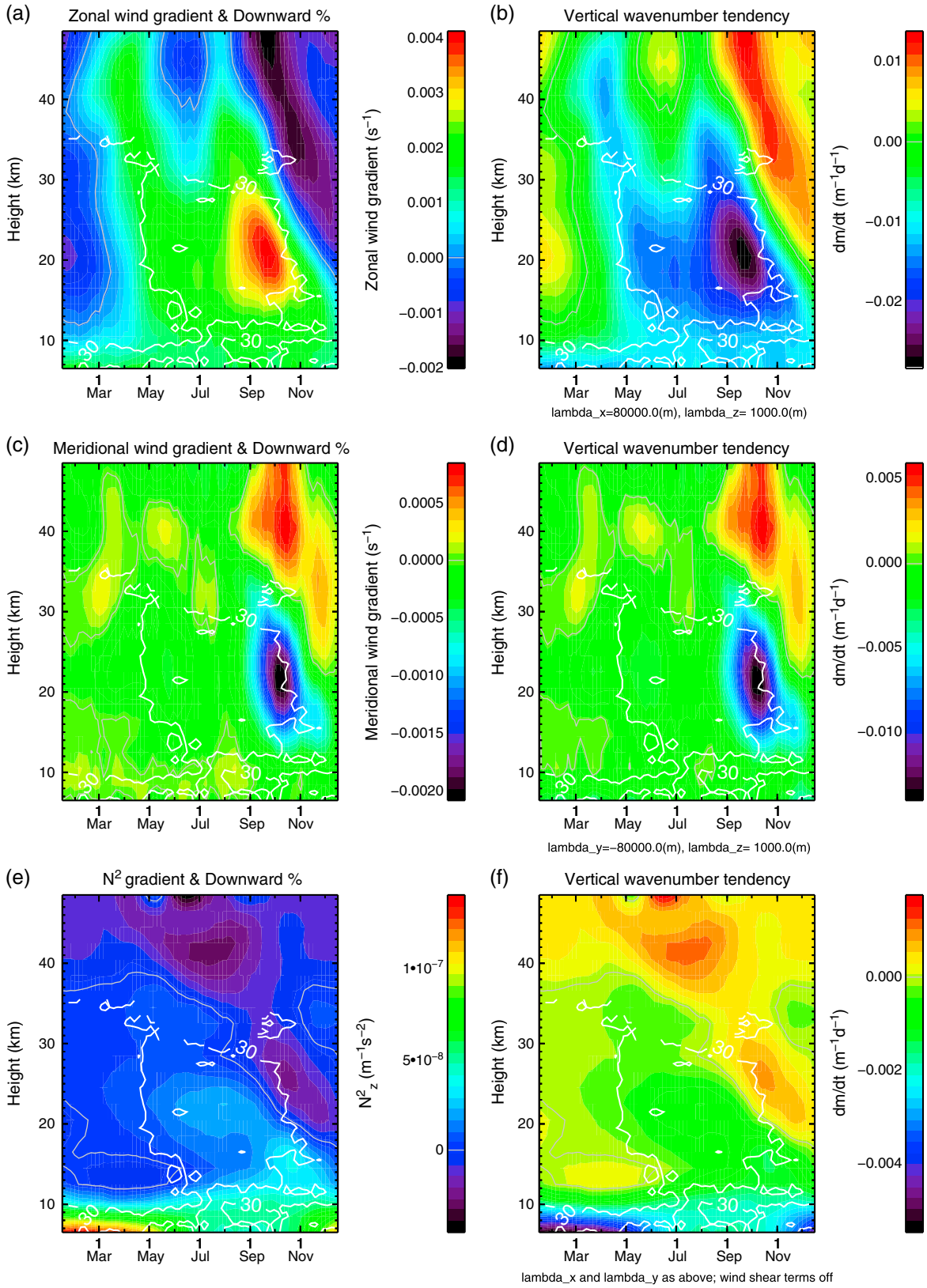

Figure 10. Vertical shear in (a) zonal wind, (c) meridional wind, and (e) Brunt Väisälä frequency squared (N_z^2) through season and height averaged over the interval 2004–2012. Tendency in vertical wave number for waves with $\lambda_x = \lambda_y = 80$ km, $\lambda_z = 1$ km are given: (b) for N_z^2 and $\overline{u}_z$ related terms, (d) for N_z^2 and $\overline{v}_z$ related terms, and (f) for only the N_z^2 related term. The 30 and 70% upward and downward propagation contours are overlaid for comparison.

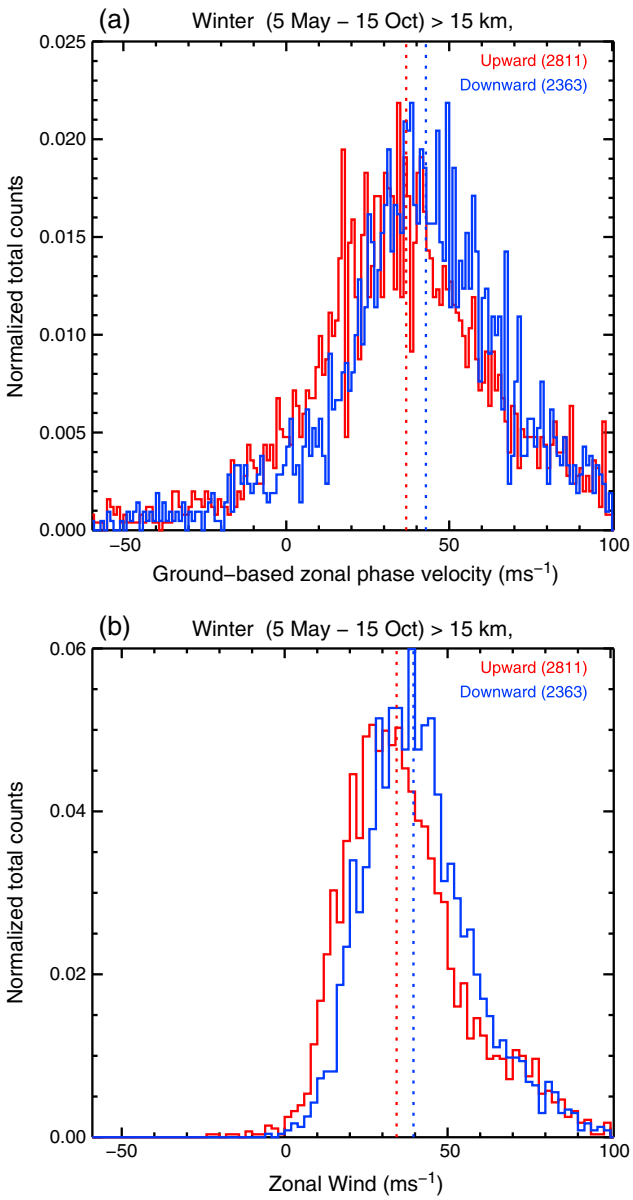

Figure 11. Occurrence histograms of the (a) ground-based zonal phase speed and (b) background zonal wind of observed wintertime gravity waves. Median values are given by vertical lines.

the ground-based zonal phase speed at the source is not known; the background wind at the height of the observation is used to infer the ground-based phase speed at the time and height that the wave is observed (see Table 3). However, a comparison of the zonal wind and the ground-based zonal phase speed distributions shown in Figure 11 (with the assumption that the ground-based zonal phase speed will not vary much during a wave's life cycle) also suggests that critical level encounters are likely. Notably, there is little potential for a typical wintertime upgoing wave to achieve a vertical wave number of zero and to be reflected (when $\hat{\omega} = N$). Thus, the downgoing waves observed are not reflected versions of the upgoing waves.

The vertical wave number tendencies following the wave due to N_z^2 and $\bar{v}_z$ effects for a wave with $k = 0$, $l = 1/80{,}000$ m^{-1}, $m = 1/1000$ m^{-1}, and $\hat{\omega} = 2.5 f_{\text{Davis}}$ are presented in Figure 10d. These tendencies are smaller than those in Figure 10b although, in September–October, there is some potential for critical level encounters described above and for reflection processes (for waves with negative l) to affect meridionally propagating waves. The vertical wave number tendency due to N_z^2-only (Figure 10f) remains small throughout the winter stratosphere (particularly when compared to its value when zonal shear effects are included).

It is noted that the parameters used in Figures 10b, 10d, and 10f will vary as the waves propagate vertically (creating the distributions shown in Figure 5 that sample much of the waves' life cycles). It is clear from this analysis though that the strongest influence on vertical wave propagation is the vertical shear in the zonal wind through the stratosphere.

4.4. Momentum Flux

Zink and Vincent [2001b] and *Alexander et al.* [2010] note that if the intrinsic frequency of a gravity wave is known, gravity wave polarization relations can be used to infer the wave momentum flux through the horizontal wind and temperature perturbations:

$$\rho\overline{u'w'}\delta_- = -\rho\frac{\hat{\omega}g}{N^2}\overline{u'\hat{T}'_{+90}}\delta_-, \tag{4}$$

$$\rho\overline{v'w'}\delta_- = -\rho\frac{\hat{\omega}g}{N^2}\overline{v'\hat{T}'_{+90}}\delta_-, \tag{5}$$

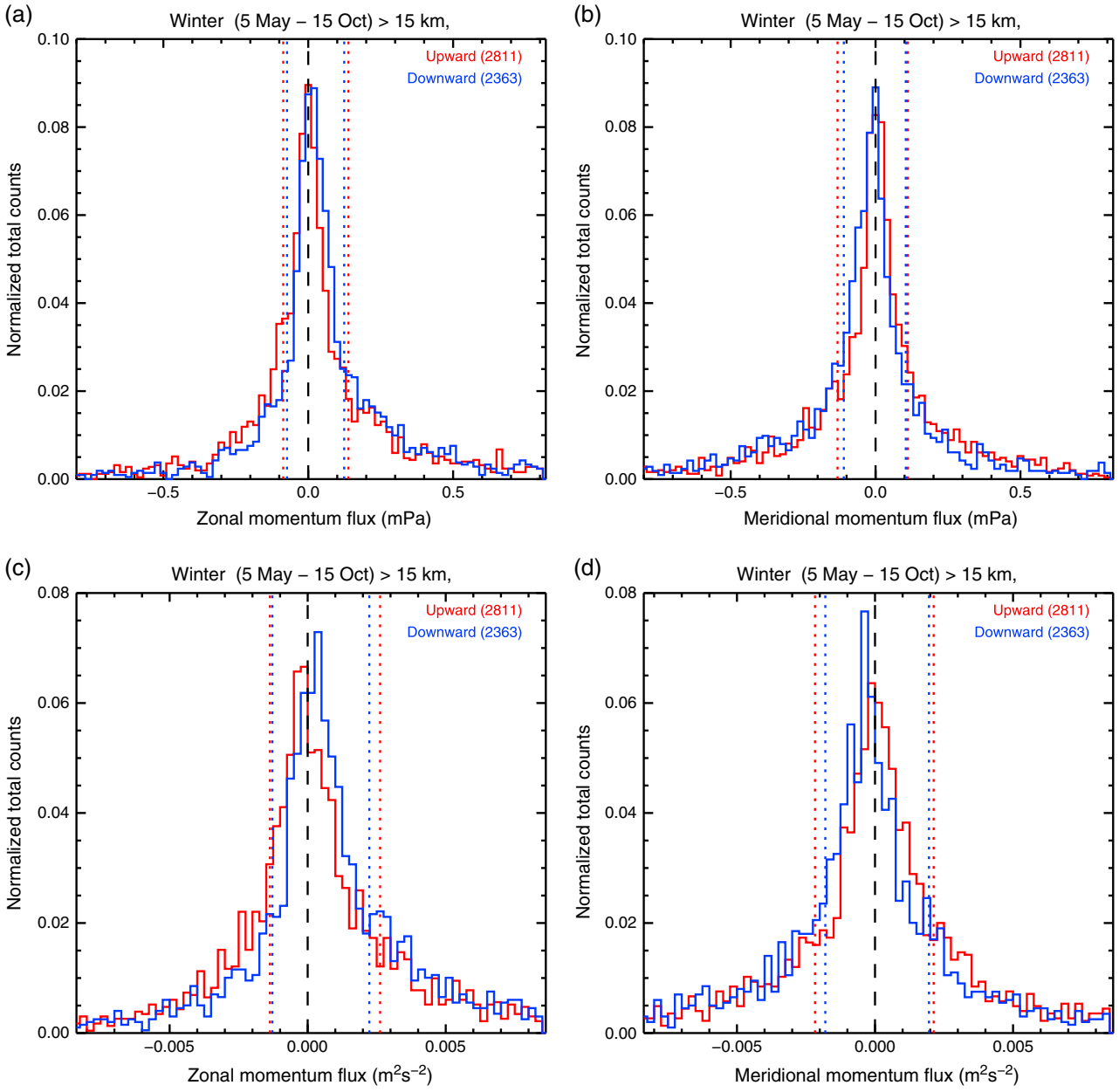

Figure 12. Occurrence histograms of the (a) zonal momentum flux ($\rho\overline{u'w'}\delta_{-}$) and (b) meridional momentum flux ($\rho\overline{v'w'}\delta_{-}$) of observed wintertime gravity waves (in mPa). Median values (of positive and negative cohorts) are given by vertical lines. (c and d) Zonal and meridional density-weighted momentum flux histograms (in $m^2\ s^{-2}$).

where $\delta_{-} = (1 - f^2/\hat{\omega}^2)$ and $\hat{T}'_{+90}$ is the 90° phase-shifted temperature perturbation profile normalized using the mean $\overline{T}$. This phase-shifted (Hilbert-transformed) temperature is a byproduct of the wavelet analysis, and the product above can easily be calculated and averaged over the vertical extent of the observed wave to provide momentum flux estimates. Density ρ is calculated using $\overline{T}$, $\overline{p}$, and the ideal gas law.

Histograms of the wintertime zonal and meridional momentum flux for waves between 15 and 31 km are presented in Figures 12a and 12b. The distributions of both components of the momentum flux are centered on zero and extend out to <1 mPa. Median values (after separation into positive and negative cohorts) are between 0.08 and 0.15 mPa. Histograms of momentum flux per unit mass ($\overline{u'w'}\delta_{-}$ and $\overline{v'w'}\delta_{-}$) are also presented (Figures 12c and 12d, in $m^2\ s^{-2}$) for comparison with other studies.

Table 4. Mean (and Median) Momentum Flux Values for Summer and Winter Between 15 and 32 km[a]

Parameter	$\rho\overline{u'w'}\delta\_$ (mPa)	$\rho\overline{v'w'}\delta\_$ (mPa)	$\overline{u'w'}\delta\_$ ($m^2\ s^{-2}$)	$\rho\overline{v'w'}\delta\_$ ($m^2\ s^{-2}$)
		Winter		
		(5 May to 15 October)		
Upward	0.24 (0.013)	0.12 (3.3×10^{-3})	4.1×10^{-3} (2.6×10^{-4})	1.9×10^{-3} (7.1×10^{-5})
Downward	0.28 (0.040)	-1.9×10^{-3} (−0.022)	4.8×10^{-3} (7.0×10^{-4})	1.9×10^{-4} (4.0×10^{-4})
All	0.26 (0.024)	0.13 (-8.3×10^{-3})	4.4×10^{-3} (4.9×10^{-4})	1.1×10^{-3} (-1.6×10^{-4})
		Summer		
		(1 November to 1 April)		
Upward	0.078 (0.022)	9.9×10^{-3} (3.1×10^{-4})	1.5×10^{-3} (4.5×10^{-4})	7.1×10^{-5} (6.1×10^{-6})
Downward	0.17 (0.014)	−0.030 (8.7×10^{-3})	2.8×10^{-3} (2.9×10^{-4})	-2.5×10^{-3} (-1.8×10^{-4})
All	0.085 (0.022)	0.069 (2.5×10^{-4})	1.6×10^{-3} (4.4×10^{-4})	-1.4×10^{-4} (5.6×10^{-6})

[a]Entries are provided for upward and downward propagating waves and both upward and downward combined.

The above values of momentum flux are small compared to those generated orographically; for example, *Alexander and Grimsdell* [2013] measure monthly mean momentum fluxes in the vicinity of sub-Antarctic islands that are more then 50 times these values. However, the relative importance of the measured inertial gravity waves will be determined by factors including source intermittency which is currently not known.

The effects of differing analysis techniques (wavelet versus nonwavelet) discussed in section 4.2 should be noted in the context of these momentum flux measurements; wavelet analysis allows the wind temperature covariance contribution of single waves to be separated out, whereas other techniques have the potential to combine contributions due to multiple waves [*Zink and Vincent*, 2001b]. Wavelets also allow the intrinsic frequency to be isolated, whereas other studies have used mean values of this quantity [*Vincent et al.*, 1997; *Yoshiki and Sato*, 2000]. *Zink and Vincent* [2001b] note that the use of the mean intrinsic frequencies almost certainly overestimates the wave fluxes.

The analysis applied here is based on *Zink and Vincent* [2001b], and despite the latitude differences, their Macquarie Island (55°S, 159°E) results provide a good reference for comparison. Average and median values of the momentum flux for Davis in winter (5 May to 15 October) and summer (1 November to 1 April) above 15 km are presented in Table 4. Macquarie Island average values in *Zink and Vincent* [2001b] are approximately 3–13 times larger but opposite in sign in the winter (including the density-weighted values). Summertime values at Davis are generally similar in magnitude but opposite in sign to Macquarie Island. *Vincent et al.* [1997] present a table of average momentum fluxes for their observations from Macquarie Island, and their results are larger than the values found here in summer and winter. As noted in *Zink and Vincent* [2001b], the difference in methods is the dominant contributor.

Yoshiki and Sato [2000] present momentum fluxes above Syowa Station calculated using a value of intrinsic frequency obtained assuming the universal spectrum with spectral index parameter $p = 2$. Note that their values of $\overline{u'w'}$ and $\overline{v'w'}$ do not include the $\delta\_$ correction applied here. Regions of momentum fluxes greater than 5×10^{-3} $m^2\ s^{-2}$ are apparent in the winter stratosphere, most widespread in $\overline{u'w'}$. These are similar to (larger than) the values given in Table 4 for zonal (meridional) momentum fluxes. The $\overline{u'w'}$ and $\overline{v'w'}$ values tabulated in *Vincent et al.* [1997] are larger, but it is noted that these use $p = 5/3$: this is shown to increase the magnitude of the momentum flux estimates.

Momentum fluxes are calculated for waves observed during a series of high time resolution radiosonde observing campaigns at Syowa in *Sato and Yoshiki* [2008]. This analysis identifies the intrinsic frequency of each wave and thus bears a similarity to the wavelet approach applied here. Many of their $\overline{u'w'}$ and $\overline{v'w'}$ values are clustered around zero and have similar values to those displayed in Figure 12; however, some occurrences of much larger values are apparent in their March and October results.

Zink and Vincent [2001b] note that the momentum fluxes of individual waves, such as those attained here, cannot be used to infer the wave-induced vertical divergence. This is because the waves identified may be Doppler shifted into or out of the observable range of the analysis at other heights and would no longer contribute to the total momentum flux. They note that ray tracing studies are needed to overcome this issue. Such studies are beyond the scope of this paper.

5. Summary and Conclusion

The wavelet form of the gravity wave radiosonde analysis described by *Zink and Vincent* [2001a] has been applied to 12 years of data obtained at Davis station. This analysis separates the wind and temperature perturbations into single wave packets allowing the contributions associated with individual waves to be investigated. A climatology of the wave characteristics is compiled. We show that the vertical propagation statistics of the inertial gravity waves preferentially selected by this analysis show strong temporal and height variations. The characteristics of the upward and downward propagating waves are described, and it is shown that they propagate close to the horizontal (as expected) and are strongly advected by the background wind in the wintertime. It was also shown that $\overline{u}_z$ has the strongest influence on vertical propagation.

Investigations of the vertical structure of the direction of wave propagation show that around half of the waves observed in the stratosphere above Davis are downgoing between early May and mid-October. Notably, this feature is distributed over the observed stratospheric height range. Based on the similarity between the upward and downward propagating waves, it is concluded that a source that is distributed across the winter stratosphere best explains the observations. Diagnostics of nonlinear balance support this argument: height-time cross sections of the nonlinear balance equation residual show coincidence with downward propagating wave statistics. Processes in the polar winter stratosphere are thus acting as a source of inertial gravity waves. Momentum flux estimates show that the waves do not carry large amounts of momentum when compared to small-island sources. However, their intermittency (and so their overall influence) remains unknown. It is also possible that waves generated by imbalance processes that are not visible to this analysis method contribute to the momentum budget of the stratosphere.

Kinetic and potential energies of the observed waves are presented and compared to other studies as are momentum flux values. It is noted that significant differences between analysis techniques exist and that these project into large variations in the magnitude of the results. Some consistency in the form of these parameters is apparent.

Recent developments in radiosonde data analysis have made the direct extraction of vertical fluctuation energies possible [*Geller and Gong*, 2010; *Gong and Geller*, 2010; *Zhang et al.*, 2012]. This has the potential to expand the instrumental filtering window of the analysis although the constraint on vertical wavelength (and its follow-on effects) could remain. Direct calculations of the momentum flux (using w' for the $\overline{u'w'}$ product) have also been made [*Zhang et al.*, 2012, 2013]. The application of these techniques to observations near the southern polar vortex will provide additional insight into the nature of waves being produced.

An extensive body of work has been accumulated in the field of gravity wave generation through adjustment processes [see, e.g., *Plougonven and Zhang*, 2013]. The results of this study show that these process are at play in the southern polar winter stratosphere. The lack of water vapor influences in this region may provide opportunities for its use as a simplified "laboratory" for gravity wave generation.

Appendix A: Stokes Parameters

The rotation of gravity wave wind vectors along the direction of propagation has suggested analysis techniques common in the study of electromagnetic waves. *Vincent and Fritts* [1987] introduced the use of Stokes parameters [e.g., *Krauss*, 1986] to describe the polarization of gravity waves. *Eckermann* [1996] discussed the use of Stokes parameters and their relationship to other analysis techniques. Numerous studies have now applied this form of analysis to wind profiles from rockets and radio sondes [e.g., *Eckermann et al.*, 1994; *Zink and Vincent*, 2001a; *Moffat-Griffin et al.*, 2011].

Given a vertical profile of zonal and meridional velocity perturbations $u'(z)$ and $v'(z)$ dominated by sinusoidal variations of the form $u'(z) = u_0(z)\cos(mz + \delta_1)$ and $v'(z) = v_0(z)\cos(mz + \delta_2)$ where u_0, v_0 are amplitudes, m is the vertical wave number, and $\delta_1(z), \delta_2(z)$ are wave phases, the Stokes parameters can be defined as [*Eckermann*, 1996]

$$I = \frac{1}{2}(\overline{u_0^2} + \overline{v_0^2}) + (\overline{u_{\text{noise}}^2} + \overline{v_{\text{noise}}^2}) = \overline{u'^2} + \overline{v'^2} \tag{A1}$$

$$D = \frac{1}{2}(\overline{u_0^2} - \overline{v_0^2}) = u'^2 - v'^2 \tag{A2}$$

$$P = \overline{u_0 v_0 \cos\delta} = 2\overline{u'v'} \tag{A3}$$

$$Q = \overline{u_0 v_0 \sin\delta} \tag{A4}$$

where u_{noise} and v_{noise} are unpolarized contributions to the profiles, $\delta = \delta_1 - \delta_2$ and the overbar denotes average over a height interval. These equations depend on the assumption that u_0, v_0 and δ are slowly varying in height relative to $2m$ and that enough wave cycles are present to ensure cosine terms average to negligible values. It was noted by *Vincent and Fritts* [1987] that it was not possible to calculate Q unless the signal is suitably monochromatic. In *Eckermann et al.* [1994] it was noted that this analysis could be extended through the use of the Hilbert transform. If we introduce $v'_H(z) = v_0(z)\sin(mz+\delta_2(z))$, a function readily available through the imaginary part of the wavelet reconstruction used in this study (and the Hilbert transform of v' with its sign reversed), it can be shown that

$$Q = \overline{u_0 v_0 \sin\delta} = 2\overline{u'v'_H} \tag{A5}$$

and Q can be calculated.

Appendix B: Extraction of Gravity Wave Parameters

The extraction of gravity wave and background wind parameters from the vertical profiles of wind and temperature is based on techniques described in *Zink and Vincent* [2001a]. The wavelet technique provides direct measurements of vertical wavelength λ_z, background wind and temperature $\{\overline{u}, \overline{v}, \overline{T}\}$, and the wind and temperature perturbation amplitudes for a wave packet centered at an altitude z_0. The gradient of the background temperature provides the Brünt-Väisälä frequency N. Stokes parameters [*Eckermann*, 1996] describe hodograph characteristics, and the resulting axial ratio and ellipse orientation provide estimates of intrinsic frequency $\hat{\omega}$, horizontal direction of propagation, and the sense (upward or downward) of the vertical propagation [*Zink and Vincent*, 2001a].

B1. Group Velocity of Low-Frequency Waves

Given the dispersion relation for low-frequency gravity waves [*Fritts and Alexander*, 2003]

$$\hat{\omega}^2 = \frac{N^2 k_h^2}{m^2} + f^2, \tag{B1}$$

where $k_h = \sqrt{k^2 + l^2}$ is the horizontal wave number along the direction of propagation, $k = 2\pi/\lambda_x$, $l = 2\pi/\lambda_y$, $m = 2\pi/\lambda_z$, and f is the inertial frequency, the horizontal wavelength k_h can be obtained:

$$k_h = \frac{m}{N}\sqrt{\hat{\omega}^2 - f^2}. \tag{B2}$$

Noting that intrinsic group velocity is defined as $\hat{c}_{gh} = \partial\hat{\omega}/\partial k_h$, or in cartesian coordinates,

$$(\hat{c}_{gx}, \hat{c}_{gy}, \hat{c}_{gz}) = \left(\frac{\partial\hat{\omega}}{\partial k}, \frac{\partial\hat{\omega}}{\partial l}, \frac{\partial\hat{\omega}}{\partial m}\right) = (c_{gx} - \overline{u}, c_{gy} - \overline{v}, c_{gz}) \tag{B3}$$

equation (B1) can be used to obtain

$$\hat{c}_{gx} = \frac{kN^2}{\hat{\omega}m^2}, \quad \hat{c}_{gy} = \frac{lN^2}{\hat{\omega}m^2}, \tag{B4}$$

and

$$\hat{c}_{gz} = -\frac{\hat{\omega}^2 - f^2}{\hat{\omega}m}. \tag{B5}$$

This expression for $\hat{c}_{gz}$ is the same as that given in *Wang et al.* [2005].

Equation (B3) implies that the orientation of the group velocity in the intrinsic frame (given by $(\hat{c}_{gx}, \hat{c}_{gy}, \hat{c}_{gz})$) will differ from that in the ground-based frame (given by (c_{gx}, c_{gy}, c_{gz})). Stokes parameter analysis gives the orientation in the intrinsic frame such that $\hat{c}_{gx} = \hat{c}_{gh}\sin\phi$ and $\hat{c}_{gy} = \hat{c}_{gh}\cos\phi$ with ϕ being measured clockwise from north.

B2. Conversion Between Intrinsic and Ground-Based Reference Frames

Although many texts consider gravity wave parameters in both the ground and background wind-based frames [e.g., *Fritts and Alexander*, 2003], it is common to align the coordinate axes with the direction of propagation of a wave. Here the wave phase speed is derived in both frames using a cartesian coordinate system. It is clear that a wave perturbation in the parameter ψ of the form

$$\psi = \psi_o \exp\left[i(kx + ly + mz - \omega t) + \frac{z}{2H}\right] \tag{B6}$$

is defined in terms of Cartesian coordinate system that is fixed relative to the ground. An alternate (intrinsic) reference frame can be defined that moves with the background wind at a given location where $\underline{u} = (u, v, 0)$ such that

$$\begin{aligned}\hat{x} &= x - ut,\\ \hat{y} &= y - vt,\\ \hat{z} &= z - wt = z,\\ \hat{t} &= t.\end{aligned}$$

Substituting these translations into (B6) and grouping time terms yield

$$\psi = \psi_o \exp\left[i\left(\hat{k}x + \hat{l}y + \hat{m}z - \left(\hat{\omega} + \hat{k}u + \hat{l}v\right)t\right) + \frac{\hat{z}}{2H}\right]. \tag{B7}$$

Comparing these two expressions for the same wave yields

$$\begin{aligned}k &= \hat{k}\\ l &= \hat{l}\\ m &= \hat{m}\\ \omega &= \hat{\omega} + \hat{k}u + \hat{l}v\\ &= \hat{\omega} + ku + lv,\end{aligned} \tag{B8}$$

the latter expression being the familiar formula for conversion between intrinsic and ground-based frequency [e.g., *Fritts and Alexander*, 2003].

B3. Ground-Based Phase Velocity

Selecting a fixed value of the phase in (B7) (e.g., zero as here) and applying a differential holding y and z constant yield

$$k\mathrm{d}x - (\hat{\omega} + ku + lv)\mathrm{d}t = 0 \tag{B9}$$

$$\frac{\mathrm{d}x}{\mathrm{d}t} = \frac{\hat{\omega}}{k} + u + \frac{l}{k}v = c_x, \tag{B10}$$

an expression for the zonal phase speed in the ground-based frame.

Similarly, differentiating holding x and z constant yields

$$\frac{\mathrm{d}y}{\mathrm{d}t} = \frac{\hat{\omega}}{l} + \frac{k}{l}u + v = c_y. \tag{B11}$$

Fritts and Alexander [2003] note that phase speed is not a vector quantity but that wave phase propagation is in the direction given by the vector (k, l, m).

Acknowledgments

Radiosonde data are archived by the Australian Bureau of Meteorology and are available on request from www.bom.gov.au. Analysis methods used to extract gravity wave parameters are described in the text, appendices, and in Tables 1–3. The authors would like to thank the many expeditioners from the Bureau of Meteorology for their tireless efforts in launching radiosondes in conditions that are often challenging. This research has been supported through Australian Antarctic Science project 4025.

References

Alexander, M. J. (1998), Interpretations of observed climatological patterns in stratospheric gravity wave variance, *J. Geophys. Res.*, *103*(D8), 8627–8640.

Alexander, M. J., and A. W. Grimsdell (2013), Seasonal cycle of orographic gravity wave occurrence above small islands in the Southern Hemisphere: Implications for effects on the general circulation, *J. Geophys. Res. Atmos.*, *118*, 11,589–11,599, doi:10.1002/2013JD020526.

Alexander, M. J., et al. (2010), Recent developments in gravity-wave effects in climate models and the global distribution of gravity-wave momentum flux from observations and models, *Q. J. R. Meteorol. Soc.*, *136*(650), 1103–1124, doi:10.1002/qj.637.

Allen, S. J., and R. A. Vincent (1995), Gravity wave activity in the lower atmosphere: Seasonal and latitudinal variations, *J. Geophys. Res.*, *100*(D1), 1327–1350.
Andrews, D. G., J. R. Holton, and C. B. Leovy (1987), *Middle Atmosphere Dynamics*, Academic Press, London.
Baumgaertner, A. J. G., and A. J. McDonald (2007), A gravity wave climatology for Antarctica compiled from Challenging Minisatellite Payload/Global Positioning System (CHAMP/GPS) radio occultations, *J. Geophys. Res.*, *112*, D05103, doi:10.1029/2006JD007504.
Butchart, N., et al. (2011), Multimodel climate and variability of the stratosphere, *J. Geophys. Res.*, *116*, D05102, doi:10.1029/2010JD014995.
Chun, H.-Y., J.-S. Goh, and Y.-H. Kim (2007), Characteristics of inertio-gravity waves revealed in rawinsonde data observed in Korea during 20 August to 5 September 2002, *J. Geophys. Res.*, *112*, D16108, doi:10.1029/2006JD008348.
Eckermann, S. D. (1996), Hodographic analysis of gravity waves: Relationships among Stokes parameters, rotary spectra and cross-spectral methods, *J. Geophys. Res.*, *101*(D14), 19,169–19,174.
Eckermann, S. D., and W. K. Hocking (1989), Effect of superposition on measurements of atmospheric gravity waves: A cautionary note and some reinterpretations, *J. Geophys. Res.*, *94*(D5), 6333–6339.
Eckermann, S. D., and R. A. Vincent (1989), Falling sphere observations of anisotropic gravity wave motions in the upper stratosphere over Australia, *Pure Appl. Geophys.*, *130*(2/3), 509–532.
Eckermann, S. D., I. Hirota, and W. K. Hocking (1994), Gravity wave and equatorial wave morphology of the stratosphere derived from long-term rocket soundings, *Q. J. R. Meteorol. Soc.*, *121*, 149–186.
Ern, M., P. Preusse, M. J. Alexander, and C. D. Warner (2004), Absolute values of gravity wave momentum flux derived from satellite data, *J. Geophys. Res.*, *109*, D20103, doi:10.1029/2004JD004752.
Fritts, D. C., and M. J. Alexander (2003), Gravity wave dynamics and effects in the middle atmosphere, *Rev. Geophys.*, *41*(1), 1003, doi:10.1029/2001RG000106.
Garcia, R. R., and B. A. Boville (1994), "Downward control" of the mean meridional circulation and temperature distribution of the polar winter stratosphere, *J. Atmos. Sci.*, *51*(15), 2238–2245.
Geller, M. A., and J. Gong (2010), Gravity wave kinetic, potential, and vertical fluctuation energies as indicators of different frequency gravity waves, *J. Geophys. Res.*, *115*, D11111, doi:10.1029/2009JD012266.
Gong, J., and M. A. Geller (2010), Vertical fluctuation energy in United States high vertical resolution radiosonde data as an indicator of convective gravity wave sources, *J. Geophys. Res.*, *115*, D11110, doi:10.1029/2009JD012265.
Guest, F. M., M. J. Reeder, C. J. Marks, and D. J. Karoly (2000), Inertia-gravity waves observed in the lower stratosphere over Macquarie Island, *J. Atmos. Sci.*, *57*, 737–752.
Hamilton, K., and R. A. Vincent (1995), High-resolution radiosonde data offer new prospects for research, *Eos Trans. AGU*, *76*(49), 497–506, doi:10.1029/95EO00308.
Hertzog, A., G. Boccara, R. A. Vincent, F. Vial, and P. Cocquerez (2008), Estimation of gravity wave momentum flux and phase speeds from quasi-Lagrangian stratospheric balloon flights. Part II: Results from the Vorcore campaign in Antarctica, *J. Atmos. Sci.*, *65*, 3056–3070, doi:10.1175/2008JAS2710.1.
Hirota, I., and T. Niki (1985), A statistical study of inertia-gravity waves in the middle atmosphere, *J. Meteorol. Soc. Jpn.*, *63*(6), 1055–1065.
Holton, J. R. (1983), The influence of gravity wave breaking on the general circulation of the middle atmosphere, *J. Atmos. Sci.*, *40*, 2497–2507.
Innis, J. L., A. R. Klekociuk, and R. A. Vincent (2004), Interstation correlation of high-latitude lower-stratosphere gravity wave activity: Evidence for planetary wave modulation of gravity waves over Antarctica, *J. Geophys. Res.*, *109*, D17106, doi:10.1029/2004JD004961.
Ki, M.-O., and H.-Y. Chun (2010), Characteristics and sources of inertia-gravity waves revealed in the KEOP-2007 radiosonde data, *Asia-Pac. J. Atmos. Sci.*, *46*(3), 261–277, doi:10.1007/s13143-010-1001-4.
Kitamura, Y., and I. Hirota (1989), Small-scale disturbances in the lower stratosphere revealed by daily rawinsonde observations, *J. Meteorol. Soc. Jpn.*, *67*(5), 817–831.
Koch, S. E., and P. B. Dorian (1988), A mesoscale gravity wave event observed during CCOPE. Part III: Wave environment and probable source mechanisms, *Mon. Weather Rev.*, *116*, 2570–2592.
Krauss, J. D. (1986), *Radio Astronomy*, 2nd ed., Cygnus-Quasar Books, Powell, Ohio.
Leena, P. P., M. Venkat Ratnam, and B. V. Krishna Murthy (2012), Inertia gravity wave characteristics and associated fluxes observed using five years of radiosonde measurements over a tropical station, *J. Atmos. Sol. Terr. Phys.*, *84-85*, 37–44, doi:10.1016/j.jastp.2012.05.004.
Lighthill, J. (1978), *Waves in Fluids*, Cambridge Univ. Press, Cambridge.
Moffat-Griffin, T., R. E. Hibbens, M. J. Jarvis, and S. R. Colwell (2011), Seasonal variations of gravity wave activity in the lower stratosphere over an Antarctic Peninsula station, *J. Geophys. Res.*, *116*, D14111, doi:10.1029/2010JD015349.
Moffat-Griffin, T., M. J. Jarvis, S. R. Colwell, A. J. Kavanagh, G. L. Manney, and W. H. Daffer (2013), Seasonal variations in the lower stratospheric gravity wave energy above the Falkland Islands, *J. Geophys. Res. Atmos.*, *118*, 10,861–10,869, doi:10.1002/jgrd.50859.
Pedlosky, J. (2003), *Waves in the Ocean and Atmosphere*, Springer, Berlin.
Pfenninger, M., A. Z. Liu, G. C. Papen, and C. S. Gardner (1999), Gravity wave characteristics in the lower atmosphere at South Pole, *J. Geophys. Res.*, *104*(D6), 5963–5984.
Plougonven, R., and F. Zhang (2007), On the forcing of inertia-gravity waves by synoptic-scale flows, *J. Atmos. Sci.*, *64*, 1737–1742, doi:10.1175/JAS3901.1.
Plougonven, R., and F. Zhang (2013), Internal gravity waves from atmospheric jets and fronts, *Rev. Geophys.*, *52*, 33–76, doi:10.1002/2012RG000419.
Plougonven, R., H. Teitelbaum, and V. Zeitlin (2003), Inertia gravity wave generation by the tropospheric midlatitude jet as given by the Fronts and Atlantic Storm-Track Experiment radio soundings, *J. Geophys. Res.*, *108*(D21), 4686, doi:10.1029/2003JD003535.
Sato, K., and M. Yoshiki (2008), Gravity wave generation around the polar vortex in the stratosphere revealed by 3-hourly radiosonde observations at Syowa Station, *J. Atmos. Sci.*, *65*, 3719–3735, doi:10.1175/2008JAS2539.1.
Sato, K., S. Tateno, S. Watanabe, and Y. Kawatani (2012), Gravity wave characteristics in the Southern Hemisphere revealed by a high-resolution middle-atmosphere general circulation model, *J. Atmos. Sci.*, *69*, 1378–1396, doi:10.1175/JAS-D-11-0101.1.
Swinbank, R., et al. (2006), Stratospheric assimilated data, *Tech. rep.*, British Atmospheric Data Centre, Oxfordshire, U. K. [Available at http://badc.nerc.ac.uk/data/assim/.]
Tateno, S., and K. Sato (2008), A study of inertia-gravity waves in the middle stratosphere based on intensive radiosonde observations, *J. Meteorol. Soc. Jpn.*, *86*(5), 719–732.
Thomas, L., R. M. Worthington, and A. J. McDonald (1999), Inertia-gravity waves in the troposphere and lower stratosphere associated with a jet stream exit region, *Ann. Geophys.*, *17*, 115–121.
Torrence, C., and G. P. Compo (1998), A practical guide to wavelet analysis, *Bull. Am. Meteorol. Soc.*, *79*(1), 61–78.

Vincent, R. A., and M. J. Alexander (2000), Gravity waves in the tropical lower stratosphere: An observational study of seasonal and interannual variability, *J. Geophys. Res.*, *105*(D14), 17,971–17,982.

Vincent, R. A., and D. C. Fritts (1987), A climatology of gravity wave motions in the mesopause region at Adelaide, Australia, *J. Atmos. Sci.*, *44*(4), 748–760.

Vincent, R. A., S. J. Allen, and S. D. Eckermann (1997), Gravity wave parameters in the lower stratosphere, in *Gravity Wave Processes: Their Parameterization in Global Climate Models, Global Environment Change*, vol. 50, edited by K. Hamilton, pp. 7–25, Springer, New York.

Vincent, R. A., A. Hertzog, G. Boccara, and F. Vial (2007), Quasi-Lagrangian superpressure balloon measurements of gravity-wave momentum fluxes in the polar stratosphere of both hemispheres, *Geophys. Res. Lett.*, *34*, L19804, doi:10.1029/2007GL031072.

Wang, L., and M. A. Geller (2003), Morphology of gravity-wave energy as observed from 4 years (1998–2001) of high vertical resolution U.S. radiosonde data, *J. Geophys. Res.*, *108*(D16), 4489, doi:10.1029/2002JD002786.

Wang, L., M. A. Geller, and M. J. Alexander (2005), Spatial and temporal variations of gravity wave parameters. Part I: Intrinsic frequency, wavelength, and vertical propagation direction, *J. Atmos. Sci.*, *62*, 125–142, doi:10.1175/JAS-3364.1.

Yoshiki, M., and K. Sato (2000), A statistical study of gravity waves in the polar regions based on operational radiosonde data, *J. Geophys. Res.*, *105*(D14), 17,995–18,011.

Yoshiki, M., N. Kizu, and K. Sato (2004), Energy enhancements of gravity waves in the Antarctic lower stratosphere associated with variations in the polar vortex and tropospheric disturbances, *J. Geophys. Res.*, *109*, D23104, doi:10.1029/2004JD004870.

Zhang, F. (2004), Generation of mesoscale gravity waves in upper-tropospheric jet-front systems, *J. Atmos. Sci.*, *61*(4), 440–457, doi:10.1175/1520-0469(2004)061<0440:GOMGWI>2.0.CO;2.

Zhang, S. D., and F. Yi (2007), Latitudinal and seasonal variations of inertial gravity wave activity in the lower atmosphere over central China, *J. Geophys. Res.*, *112*, D05109, doi:10.1029/2006JD007487.

Zhang, S. D., F. Yi, C. M. Huang, and K. M. Huang (2012), High vertical resolution analyses of gravity wave and turbulence at a midlatitude station, *J. Geophys. Res.*, *117*, D02103, doi:10.1029/2011JD016587.

Zhang, S. D., F. Yi, C. M. Huang, K. M. Huang, Q. Gan, Y. H. Zhang, and Y. Gong (2013), Latitudinal and altitudinal variability of lower atmospheric inertial gravity waves revealed by U.S. radiosonde data, *J. Geophys. Res. Atmos.*, *118*, 7750–7764, doi:10.1002/jgrd.50623.

Zink, F. (2000), Gravity waves and turbulence in the lower atmosphere, PhD thesis, University of Adelaide, Adelaide, South Australia.

Zink, F., and R. A. Vincent (2001a), Wavelet analysis of stratospheric gravity wave packets over Macquarie Island 1. Wave parameters, *J. Geophys. Res.*, *106*(D10), 10,275–10,288.

Zink, F., and R. A. Vincent (2001b), Wavelet analysis of stratospheric gravity wave packets over macquarie island 2. Intermittency and mean-flow accelerations, *J. Geophys. Res.*, *106*(D10), 10,289–10,297.